

Automated assessment of residual plots with computer vision models

Weihao Li^a, Dianne Cook^a, Emi Tanaka^{b,c}, Susan VanderPlas^d, Klaus Ackermann^a

^aDepartment of Econometrics and Business Statistics, Monash University, Clayton, VIC, Australia;

^bBiological Data Science Institute, Australian National University, Acton, ACT, Australia;

^cResearch School of Finance, Actuarial Studies and Statistics, Australian National University, Acton, ACT, Australia; ^dDepartment of Statistics, University of Nebraska, Lincoln, Nebraska, USA

ARTICLE HISTORY

Compiled May 28, 2024

ABSTRACT

Plotting residuals is a standard practice in linear regression diagnostics, essential for identifying deviations from model assumptions such as linearity, homoscedasticity, and normality. Visual inference provides an inferential framework to assess whether residual plots contain patterns inconsistent with model assumptions, typically using a lineup protocol. However, the lineup protocol's reliance on human judgment limits its scalability. This study addresses this limitation by automating the interpretation of residual plots using computer vision models. We develop a distance measure based on Kullback-Leibler divergence to quantify the disparity between the residual distribution of a fitted classical normal linear regression model and the reference distribution. We propose a computer vision model to estimate this distance from residual plots, facilitating formal statistical testing and bootstrapping techniques to assess model specification. Our computer vision model shows strong performance, though it performs slightly less effectively on non-linearity visual patterns. The statistical tests based on the estimated distance exhibit lower sensitivity than conventional tests but higher sensitivity than human visual tests. Examples demonstrate the method's effectiveness across different scenarios, highlighting its value in automating the diagnostic process and supplementing traditional methods.

CONTACT Weihao Li. Email: weihao.li@monash.edu, Dianne Cook. Email: dcook@monash.edu, Emi Tanaka. Email: emi.tanaka@anu.edu.au, Susan VanderPlas. Email: susan.vanderplas@unl.edu, Klaus Ackermann. Email: Klaus.Ackermann@monash.edu

KEYWORDS

TBD

1. Introduction

Plotting residuals is commonly regarded as a standard practice in linear regression diagnostics (see Cook and Weisberg 1982; Belsley, Kuh, and Welsch 1980). This visual assessment plays a crucial role in identifying deviations from model assumptions, such as linearity, homoscedasticity, and normality. It also helps in understanding the goodness of fit and various characteristics of the model.

Generating a residual plot in most statistical software is often as straightforward as executing a line of code or clicking a button. However, accurately interpreting a residual plot can be challenging. A residual plot can exhibit various visual features, but it is crucial to recognize that some may arise from the characteristics of predictors and the inherent randomness of the error, rather than indicating a violation of model assumptions (Li et al. 2023). Consider Figure 1 as an example, the residuals display a triangular shape pointing to the left. While this might suggest heteroskedasticity, it is important to avoid over-interpreting this visual pattern. In this case, the fitted regression model is correctly specified, and the triangular shape is actually a result of the skewed distribution of the predictors, rather than indicating a flaw in the model.

The concept of visual inference, as proposed by Buja et al. (2009), provides an inferential framework to assess whether residual plots indeed contain visual patterns inconsistent with the model assumptions. The fundamental idea involves testing whether the true residual plot visually differs significantly from null plots, where null plots are plotted with residuals generated from the residual rotation distribution (Langsrud 2005), which is a distribution consistent with the null hypothesis H_0 that the linear regression model is correctly specified. Typically, the visual test is accomplished through the lineup protocol, where the real residual plot is embedded within a lineup alongside several null plots. If the real residual plot can be distinguished from the lineup, it provides evidence for rejecting H_0 .

The practice of delivering a residual plot as a lineup is generally regarded as a

valuable approach. Beyond its application in residual diagnostics, the lineup protocol has integrated into the analysis of diverse subjects. For instance, Loy and Hofmann (2013, 2014, 2015) illustrated its applicability in diagnosing hierarchical linear models. Additionally, Widen et al. (2016) demonstrated its utility in geographical research, while Krishnan and Hofmann (2021) explored its effectiveness in forensic examinations.

However, as pointed out by Li et al. (2023), a primary limitation of the lineup protocol lies in its reliance on human judgments. Unlike conventional statistical tests that can be performed computationally in statistical software, the lineup protocol requires human evaluation of images. This characteristic makes it less suitable for large-scale applications, given the associated high labour costs and time requirements.

There is a substantial need to develop an approach that alleviates analysts' work-load by automating repetitive tasks and providing standardized results in a controlled environment. The large-scale evaluation of lineups is impractical without the use of technology and machines.

The utilization of computers to interpret data plots has a rich history, with early efforts such as "Scagnostics" by Tukey and Tukey (1985), focusing on scatter plot diagnostics. Wilkinson, Anand, and Grossman (2005) expanded on this work, introducing graph theoretic scagnostics, which encompassed computable measures applied to planar proximity graphs. These measures, including, but not limited to, "Outlying", "Skinny", "Stringy", "Straight", "Monotonic", "Skewed", "Clumpy", and "Striated" aimed to characterize outliers, shape, density, trend, coherence and other characteristics of the data. While this approach has been inspiring, there is a recognition (Buja et al. 2009) that it may not capture all the necessary visual features that differentiate true residual plots from null plots. A more promising alternative entails enabling machines to learn the function for extracting visual features from residual plots. Essentially, this means empowering computers to discern the crucial visual features for residual diagnostics and determining the method to extract them.

Modern computer vision models are well-suited for addressing this challenge. They rely on deep neural networks with convolutional layers (Fukushima and Miyake 1982). These layers leverage hierarchical patterns in data, downsizing and transforming images by summarizing information in a small space. Numerous studies have demon-

strated the efficacy of convolutional layers in addressing various vision tasks, including image recognition (Rawat and Wang 2017). Despite the widespread use of computer vision models in fields like computer-aided diagnosis (Lee and Chen 2015), pedestrian detection (Brunetti et al. 2018), and facial recognition (Emami and Suciu 2012), their application in reading data plots remains limited. While some studies have explored the use of computer vision models for tasks such as reading recurrence plots for time series regression (Ojeda, Solano, and Peramo 2020), time series classification (Chu et al. 2019; Hailesilassie 2019; Hatami, Gavet, and Debayle 2018; Zhang et al. 2020), anomaly detection (Chen, Su, and Yang 2020), and pairwise causality analysis (Singh et al. 2017), the application of reading residual plots with computer vision models represents a relatively new field of study.

In this paper, we develop computer vision models and integrate them into the residual plots diagnostics workflow, addressing the need for automated visual inference. The paper is structured as follows. Section 2 discusses various specifications of the computer vision models. Section 3 defines the distance measure used to measure model violations. Section 4 explains how the computer vision models estimate this distance measure. Section 6 covers the statistical testing based on the estimated distance. Sections 7, 8, and 9 detail the data preparation, model architecture, and training process, respectively. The results are presented in Section 10. Finally, we conclude with a discussion of our findings and propose ideas for future research directions.

2. Model Specifications

There are various specifications of the computer vision model that can be used to assess residual plots. We discuss these specifications below focusing on two key components of the model formula: the input and the output format.

2.1. *Input Formats*

Deep learning models are in general very sensitive to the input data. The quality and relevance of the input data greatly influence the model’s capacity to generate insightful and meaningful results. There are several designs of the input format can

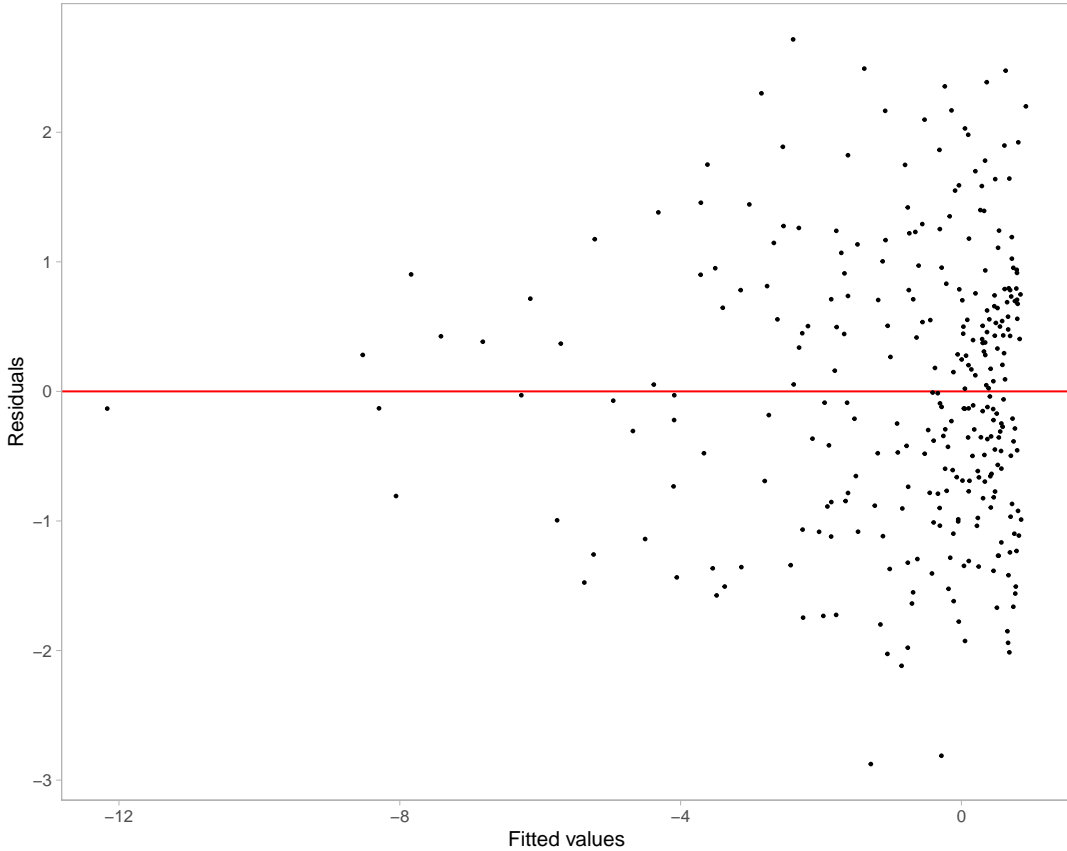


Figure 1. An example residual vs fitted values plot (red line indicates 0). The vertical spread of the data points varies with the fitted values. This often indicates the existence of heteroskedasticity. The Breusch-Pagan test rejects this residual plot at 95% significance level (p -value = 0.046).

be considered.

A straightforward design involves feeding a vector of residuals along with a vector of fitted values, essentially providing all the necessary information for creating a residuals vs fitted values plot. However, a drawback of this method is the dynamic input size, which changes based on the number of observations. For modern computer vision models implemented in mainstream software like TensorFlow (Abadi et al. 2016), the input shape is typically fixed. One solution is to pad the input vectors with leading or trailing zeros when the input tensor expects longer vectors, but it may fail if the input vector surpasses the designed length. Another strategy is to summarize the residuals and fitted values separately using histograms and utilize the counts as the input. By controlling the number of bins in the histograms, it becomes possible to provide fixed-length input vectors. Still, since histograms only capture the marginal distribution of residuals and fitted values respectively, they can not be used to differentiate visual

patterns with same marginal distributions but different joint distributions.

Another design involves using an image as input. The primary advantage of this design, as opposed to the vector format, is the availability of the existing and sophisticated image processing architectures developed over the years, such as the VGG16 architecture proposed in Simonyan and Zisserman (2014). These architectures can effectively capture and summarize spatial information from nearby pixels, which is less straightforward with vector input. The main considerations are the image resolution and the aesthetics of the residual plot. In general, higher resolution provides more information to the model but comes with the trade-off of increased complexity and greater difficulty in training. As for the aesthetics of the residual plot, a practical solution is to consistently present residual plots in the same style to the model. This implies that the model can not accept arbitrary images as input but requires the use of the same pre-processing pipeline to convert residuals and fitted values into a standardized-style residual plot.

Providing multiple residual plots to the model, such as a pair of plots, a triplet or a lineup is also a possible option. Chopra, Hadsell, and LeCun (2005) have shown that computer vision models designed for image comparison can assess whether a pair of images are similar or dissimilar. Applied to our specific problem, we can define null plots of a fitted regression model to be similar to each other, while considering true residual plots to be distinct from null plots of any fitted regression model. A triplet constitutes a set of three images, denoted as $image_1$, $image_2$ and $image_3$. It is often used to predict whether $image_2$ or $image_3$ is more similar to $image_1$, proving particularly useful for establishing rankings between samples. For this setup, we can apply the same criteria to define similarity between images. However, it is important to note that these two approaches usually require additional considerations regarding the loss function and, at times, non-standard training processes due to shared weights between different convolutional blocks.

Presenting a lineup to a model aligns closely with the lineup protocol. However, as the number of residual plots in a lineup increases, the resolution of the input image grows rapidly, posing challenges in training the model. We experimented with this approach in a pilot study, but the performance of the trained model was sub-optimal.

We did not explore all the mentioned input formats due to the significant costs tied to data preparation and model training. Taking into account the implementation cost and the need for model interpretability, we settled on the single residual plot input format.

2.2. *Output Formats*

Given that the input is a single residual plot represented as a fixed-resolution image, the output from the computer vision model can take one of two forms: binary or numeric. This choice determines whether the model belongs to a classification model or a regression model. The binary outcome encoded as 0 and 1 could be used to represent whether the input image is a null plot, or whether the input image would be rejected in a visual test conducted by humans. Training a model following the latter option requires data from prior human subject experiments, presenting difficulties in controlling the quality of data due to variations in experimental settings across different studies. Additionally, some visual inference experiments are unrelated to linear regression models or residual plot diagnostics, resulting in a limited amount of available training data.

Alternatively, the output could be a meaningful and interpretable numerical measure useful for assessing residual plots, such as the strength of suspicious visual patterns reflecting the extent of model violations, or the difficulty index for identifying whether a residual plot has no issues. However, these numeric measures are often informally used in daily communication but are not typically formalized or rigorously defined. For the purpose of training a model, this numeric measure has to be quantifiable.

In this study, we chose to define and use a distance measure to quantify the difference between the residual plot and the null plots. Vo and Hays (2016) have also demonstrated that defining a proper distance between images can enhance the matching accuracy in image search compared to a binary outcome model.

3. Distance Between Residual Plots

In a visual test, the observer will be asked to choose one or more plots that stand out as most distinct from others in a given lineup. To develop a computer vision model for assessing residual plots within the visual inference framework, it is important to precisely define a numerical measure of “difference” or “distance” between plots. This distance can take the form of a basic statistical operation on pixels, such as the sum of square differences. Alternatively, it could involve established image similarity metrics like the Structural Similarity Index Measure (Wang et al. 2004). The challenge lies in the fact that metrics tailored for image comparison may not be suitable for evaluating data plots, where only essential plot elements require assessment (Chowdhury et al. 2018). Furthermore, scagnostics mentioned in Section 1 could be used to construct distance measures for residual plots comparison, but the functional form still needs to be carefully refined to accurately reflect the extent of the violations.

3.1. *Residual Distribution*

The distance measure proposed in this study takes into account the fact that we tried to measure how different a residual plot is from a good residual plot, or in other words, how different a given fitted regression model is from a correctly specified model.

For a classical normal linear regression model, residuals e are derived from the fitted values \hat{y} and observed values y . Suppose the data generating process is known and the regression model is correctly specified, by the Frisch-Waugh-Lowell theorem (Frisch and Waugh 1933), residuals e can also be treated as random variables and written as a linear transformation of the error ε formulated as $e = \mathbf{R}\varepsilon$, where $\mathbf{R} = \mathbf{I}_n - \mathbf{X}(\mathbf{X}'\mathbf{X})^{-1}\mathbf{X}'$ is the residual operator and an idempotent matrix, \mathbf{X} is the design matrix, \mathbf{I}_n is a n by n identity matrix, and n is the number of observations.

One of the assumptions of the classical normal linear regression model is the error ε follows a multivariate normal distribution with zero mean and constant variance, i.e., $\varepsilon \sim N(\mathbf{0}_n, \sigma^2 \mathbf{I}_n)$. It can be known that residuals e also follow a certain probability distribution transformed from the multivariate normal distribution, which will be denoted as Q . This reference distribution Q summarizes what good residuals should

follow given the design matrix \mathbf{X} is known and fixed.

Suppose the design matrix \mathbf{X} has linearly independent columns, the trace of the hat matrix will equal to the number of columns in \mathbf{X} denoted as k . As a result, the rank of \mathbf{R} is $n - k$, and Q is a degenerate multivariate distribution. To capture the characteristics of Q , such as moments, we can simulate a large numbers of $\boldsymbol{\varepsilon}$ and transform it to \mathbf{e} to get the empirical estimates. For simplicity, in this study, we replaced the variance-covariance matrix of residuals $\text{cov}(\mathbf{e}, \mathbf{e}) = \mathbf{R}\sigma^2\mathbf{R}' = \mathbf{R}\sigma^2$ with a full-rank diagonal matrix $\text{diag}(\mathbf{R}\sigma^2)$, where $\text{diag}(\cdot)$ sets the non-diagonal entries of a matrix to zeros. The resulting distribution for \mathbf{Q} is $N(\mathbf{0}_n, \text{diag}(\mathbf{R}\sigma^2))$.

Distribution Q is derived from the correctly specified model. However, if the model is misspecified, then the actual distribution of residuals denoted as P , will be different from Q . For example, if the data generating process contains variables correlated with any column of \mathbf{X} but missing from \mathbf{X} , causing an omitted variable problem, P will be different from Q because the residual operator obtained from the fitted regression model will not be the same as \mathbf{R} . Besides, if the $\boldsymbol{\varepsilon}$ follows a non-normal distribution such as a multivariate lognormal distribution, P will usually be skewed and has a long tail.

3.2. *Distance of P from Q*

Define a proper distance between distributions is usually easier than define a proper distance between data plots. Given the true residual distribution Q and the reference residual distribution P , we used a distance measure based on Kullback-Leibler divergence (Kullback and Leibler 1951) to quantify the difference between two distributions

$$D = \log(1 + D_{KL}), \quad (1)$$

$$D_{KL} = \int_{\mathbb{R}^n} \log \frac{p(\mathbf{e})}{q(\mathbf{e})} p(\mathbf{e}) d\mathbf{e}, \quad (2)$$

where $p(\cdot)$ and $q(\cdot)$ are the probability density functions for distribution P and distribution Q respectively.

This distance measure was first proposed in Li et al. (2023). It was mainly designed for measuring the effect size of non-linearity and heteroskedasticity in a residual plot. Li et al. (2023) have derived that, for a classical normal linear regression model that omits a necessary higher-order predictors \mathbf{Z} , and incorrectly assumes $\boldsymbol{\varepsilon} \sim N(\mathbf{0}_n, \sigma^2 \mathbf{I}_n)$ while in fact $\boldsymbol{\varepsilon} \sim N(\mathbf{0}_n, \mathbf{V})$ with \mathbf{V} being an arbitrary symmetric positive semi-definite matrix, Q can be represented as $N(\mathbf{R}\mathbf{Z}\boldsymbol{\beta}_z, \text{diag}(\mathbf{R}\mathbf{V}\mathbf{R}))$. Note that the variance-covariance matrix is replaced with the diagonal matrix to ensure it is a full-rank matrix.

Since both P and Q are adjusted to be multivariate normal distributions, equation 2 can be further expanded to

$$D_{KL} = \frac{1}{2} \left(\log \frac{|\text{diag}(\mathbf{W})|}{|\text{diag}(\mathbf{R}\sigma^2)|} - n + \text{tr}(\text{diag}(\mathbf{W})^{-1} \text{diag}(\mathbf{R}\sigma^2)) + \boldsymbol{\mu}'_z (\text{diag}(\mathbf{W}))^{-1} \boldsymbol{\mu}_z \right), \quad (3)$$

where $\boldsymbol{\mu}_z = \mathbf{R}\mathbf{Z}\boldsymbol{\beta}_z$, and $\mathbf{W} = \mathbf{R}\mathbf{V}\mathbf{R}$. The assumed error variance σ^2 is set to be $\text{tr}(\mathbf{V})/n$, which is the expectation of the estimated variance.

3.3. Non-normal P

For non-normal error $\boldsymbol{\varepsilon}$, the true residual distribution P is unlikely to be a multivariate normal distribution. Thus, equation 3 given in Li et al. (2023) will not be applicable to models violating the normality assumption.

To evaluate the Kullback-Leibler divergence of non-normal P from Q , the fallback is to solve equation 2 numerically. However, since \mathbf{e} is a linear transformation of non-normal random variables, it is very common that the general form of P is unknown, meaning that we can not easily compute $p(\mathbf{e})$ using a well-known probability density function. Additionally, even if $p(\mathbf{e})$ can be calculated for any $\mathbf{e} \in \mathbb{R}^n$, it will be very difficult to do numerical integration over the n dimensional space, because n could be potentially very large.

In order to approximate D_{KL} in a practically computable manner, the elements of

\mathbf{e} are assumed to be independent of each other. This assumption solves both of the issues mentioned above. First, we no longer need to integrate over n random variables. The result of equation 2 is now the sum of the Kullback-Leibler divergence evaluated for each individual residual thanks for the independence assumption. Second, it is not required to know the joint probability density $p(\mathbf{e})$ any more. Instead, the evaluation of Kullback-Leibler divergence for an individual residual relies on the knowledge of the marginal density $p_i(e_i)$, where e_i is the i -th residual for $i = 1, \dots, n$. This is much easier to approximate through simulation. It is also worth mentioning that this independence assumption generally will not hold, since $\text{cov}(e_i, e_j) \neq 0$ if $\mathbf{R}_{ij} \neq 0$ for any $1 \leq i < j \leq n$, but its existence is essential for reducing the computational cost.

Given \mathbf{X} and β , the algorithm for approximating equation 2 starts from simulating m sets of observed values \mathbf{y} according to the data generating process. The observed values are stored in a matrix \mathbf{A} with n rows and m columns, where each column of \mathbf{A} is a set of observed values. Then, we can get m sets of realized values of \mathbf{e} stored in the matrix \mathbf{B} by applying the residual operator $\mathbf{B} = \mathbf{RA}$. Furthermore, kernel density estimation (KDE) with Gaussian kernel and optimal bandwidth selected by the Silverman's rule of thumb (Silverman 2018) is applied on each row of B to estimate $p_i(e_i)$ for $i = 1, \dots, n$. The KDE computation can be done by the `density` function in R.

Since the Kullback-Leibler divergence can be viewed as the expectation of the log-likelihood ratio between distribution P and distribution Q evaluated on distribution P , we can reuse the simulated residuals in matrix \mathbf{B} to estimate the expectation by the sample mean. With the independence assumption, for non-normal P , D_{KL} can be approximated by

$$D_{KL} \approx \sum_{i=1}^n \hat{D}_{KL}^{(i)}, \quad (4)$$

$$\hat{D}_{KL}^{(i)} = \frac{1}{m} \sum_{j=1}^m \log \frac{\hat{p}_i(B_{ij})}{q(B_{ij})}, \quad (5)$$

where $\hat{D}_{KL}^{(i)}$ is the estimator of the Kullback-Leibler divergence for an individual resid-

ual e_i , B_{ij} is the i -th row and j -th column entry of the matrix B , $\hat{p}_i(\cdot)$ is the kernel density estimator of $p_i(\cdot)$, $q(\cdot)$ is the normal density function with mean zero and an assumed variance estimated as $\widehat{\sigma^2} = \sum_{b \in \text{vec}(B)} (b - \sum_{b \in \text{vec}(B)} b/nm)^2/(nm - 1)$, and $\text{vec}(\cdot)$ is the vectorization operator which turns a $n \times m$ matrix into a $nm \times 1$ column vector by stacking the columns of the matrix on top of each other.

4. Distance Estimation

In the previous sections, we have defined a distance measure given in equation 1 for quantifying the difference between the true residual distribution P and an ideal reference distribution Q . It can be noticed that this distance measure can only be computed when the data generating process is known. In reality, we often have no knowledge about the data generating process, otherwise we do not need to fit a linear regression model in the first place.

We tried to train a computer vision model to estimate this distance measure with a residual plot. Let D be the result of equation 1, and our estimator \hat{D} is formulated as

$$\hat{D} = f_{CV}(V_{h \times w}(\mathbf{e}, \hat{\mathbf{y}})), \quad (6)$$

where $V_{h \times w}(\cdot)$ is a plotting function that saves a residuals vs fitted values plot with fixed aesthetic as an RGB image with $h \times w$ pixels, $f_{CV}(\cdot)$ is a computer vision model which takes an $h \times w$ image as input and predicts the distance in the domain $[0, +\infty)$.

With the estimated distance \hat{D} , we will be able to know how different the underlying distribution of the residuals is from a good residual distribution. \hat{D} can also be used as an index of the model violations indicating the strength of the visual signal embedded in the residual plot.

It is not expected that \hat{D} will be equal to original distance D . This is largely because information contained in a single residual plot is limited and it may not be able to summarise all the important characteristics of the residual distribution. For a given residual distribution P , many different residual plots can be simulated, where many

will share similar visual patterns, but some of them could be visually very different from the rest, especially for regression models with small n . This suggests the error of the estimation will vary depends on whether the input residual plot is representative or not.

5. Model Violations Index (MVI)

\hat{D} is an estimator of the difference between the true residual distribution and the reference residual distribution. This difference primarily arises from deviations in model assumptions. The magnitude of D directly reflects the degree of these deviations, thus making \hat{D} instrumental in forming a model violations index.

Note that Equation 1 might be influenced by the number of random variables involved in its evaluation. Generally, a larger number of observations will lead to a greater distance D . However, this does not imply that \hat{D} fails to accurately represent the extent of model violations. In fact, when examining residual plots with more observations, we often observe a stronger visual signal strength, as the underlying patterns are more likely to be revealed, except in cases of significant overlapping.

For a consistent data generating process, D typically increases logarithmically with the number of observations. This behaviour comes from the relationship $D = \log(1 + D_{KL})$, where $D_{KL} = \sum_{i=1}^n D_{KL}^{(i)}$ under the assumption of independence.

Therefore, the Model Violations Index (MVI) can be proposed as

$$\text{MVI} = C + \hat{D} - \log(n), \quad (7)$$

where C is a large enough constant keeping the result positive.

Figures 2 and 3 display the residual plots for fitted models exhibiting varying degrees of non-linearity and heteroskedasticity. Each residual plot's MVI is computed using Equation 7 with $C = 10$. When $\text{MVI} > 8$, the visual patterns are notably strong and easily discernible by humans. In the range $6 < \text{MVI} < 8$, the visibility of the visual pattern diminishes as MVI decreases. Conversely, when $\text{MVI} < 6$, the visual

Table 1. Degree of model violations or the strength of the visual signals according to the Model Violation Index (MVI). The constant C is set to be 10.

Degree of model violations	Range ($C = 10$)
Strong	$MVI > 8$
Moderate	$6 < MVI < 8$
Weak	$MVI < 6$

pattern tends to become relatively faint and challenging to observe. Table 1 provides a summary of the MVI usage and it is applicable to other linear regression models.

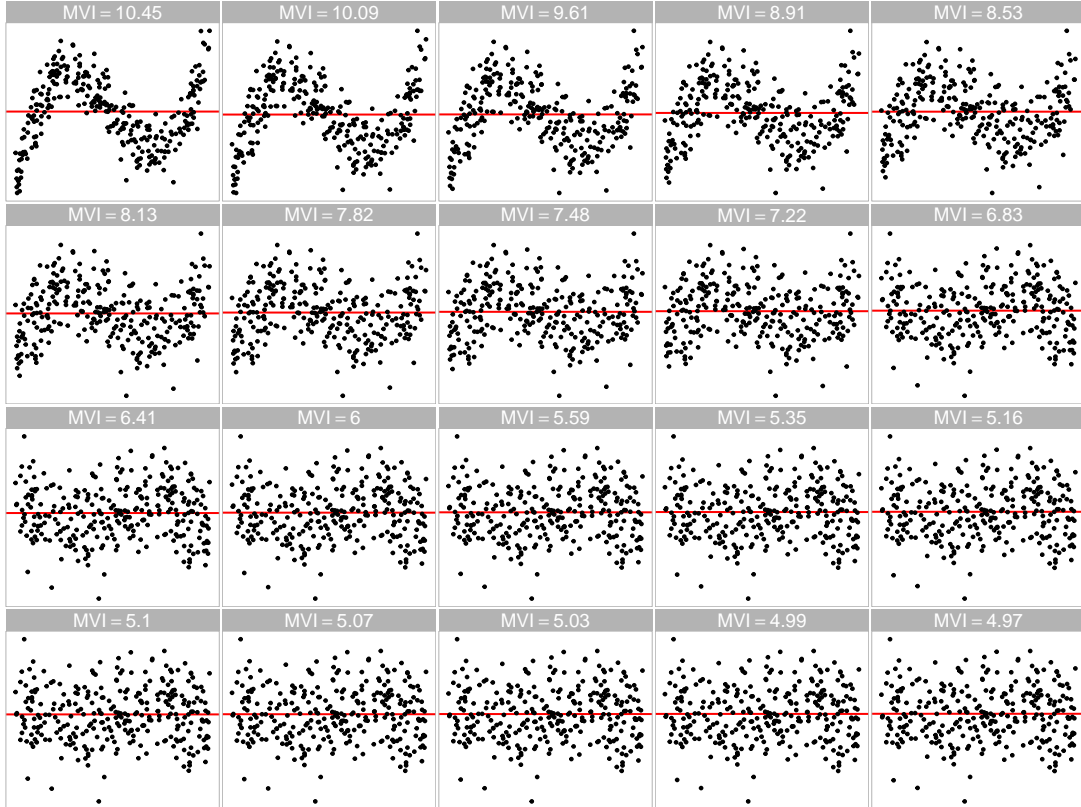


Figure 2. Residual plots generated from fitted models exhibiting varying degrees of non-linearity violations. The Model violations index (MVI) is displayed atop each residual plot. The non-linearity patterns are relatively strong for $MVI > 8$, and relatively weak for $MVI < 6$.

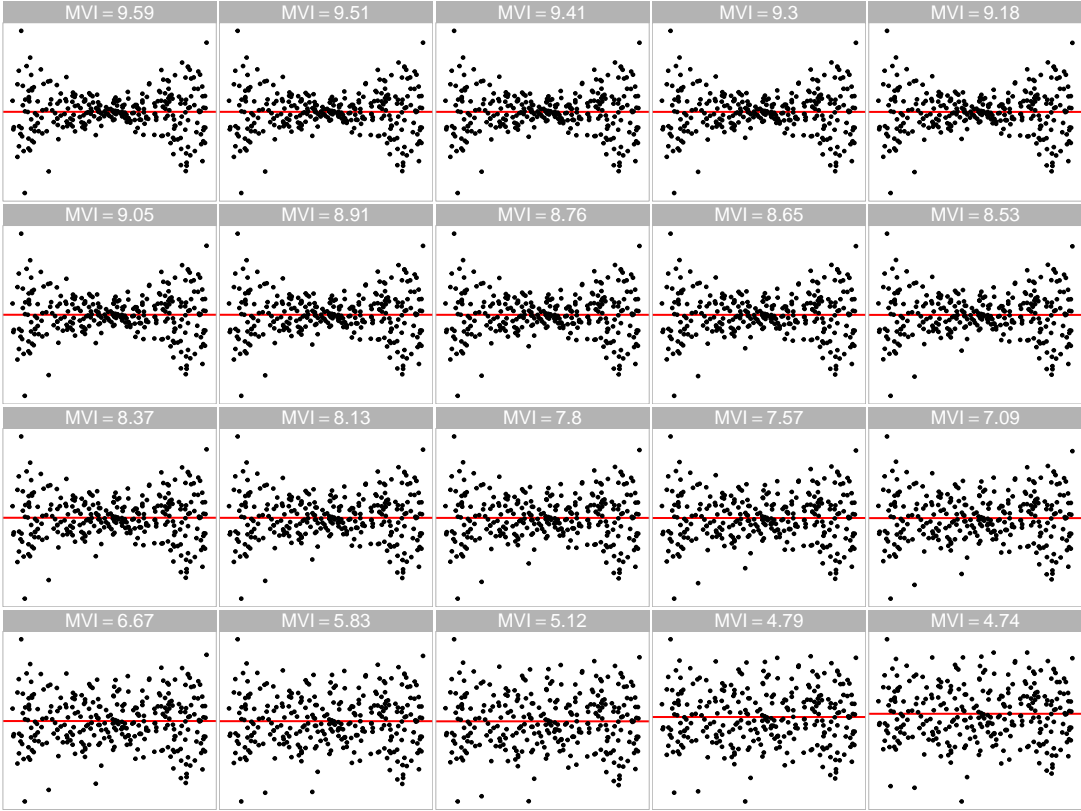


Figure 3. Residual plots generated from fitted models exhibiting varying degrees of heteroskedasticity violations. The Model violations index (MVI) is displayed atop each residual plot. The heteroskedasticity patterns are relatively strong for $MVI > 8$, and relatively weak for $MVI < 6$.

6. Statistical testing

6.1. Lineup Evaluation

Theoretically, the distance D for a correctly specified model is 0, because P will be the same as Q . However, the computer vision model may not necessarily predict 0 for a null plot. Using Figure 1 as an example, it contains a visual pattern which is an indication of heteroskedasticity. We would not expect the model to be able to magically tell if the suspicious pattern is caused by the skewed distribution of the fitted values or the existence of heteroskedasticity. Additionally, some null plots could have outliers or strong visual patterns due to randomness, and a reasonable model will try to summarise those information into the prediction, resulting in $\hat{D} > 0$.

This property is not an issue if $\hat{D} \gg 0$ for which the visual signal of the residual plot is very strong, and we usually do not need any further examination of the significance of the result. However, if the visual pattern is weak or moderate, having \hat{D} will not be

sufficient to determine if H_0 should be rejected.

To address this issue while adhering to the principle of visual inference, we can compare the estimated distance \hat{D} to the estimated distances for the null plots in a lineup. Specifically, if a lineup comprises 20 plots, the null hypothesis H_0 will be rejected if \hat{D} exceeds the maximum estimated distance among the $m - 1$ null plots, denoted as $\max_{1 \leq i \leq m-1} \hat{D}_{null}^{(i)}$, where $\hat{D}_{null}^{(i)}$ represents the estimated distance for the i -th null plot. This approach is equivalent to the typical lineup protocol requiring a 95% significance level, where H_0 is rejected if the data plot is identified as the most distinct plot by the sole observer. The estimated distance serves as a metric to quantify the difference between the data plot and the null plots, as intended.

For lineups consisting of more than 20 plots, the 95% significance level can be maintained if the number of plots is a multiple of 20. Specifically, for lineups comprising $20t$ plots, where t is a positive integer, we reject H_0 if \hat{D} exceeds 95% $\hat{D}_{null}^{(i)}$ for $i = 1, \dots, 20t - 1$. The p -value in this case is given by $\frac{1}{20t} + \frac{1}{20t} \sum_{i=1}^{20t-1} I(\hat{D}_{null}^{(i)} > \hat{D})$, where $I(\cdot)$ is the indicator function.

Moreover, if the number of plots in a lineup, denoted by m , is sufficiently large, the empirical distribution of $\hat{D}_{null}^{(i)}$ can be viewed as an approximation of the null distribution of the estimated distance. Consequently, quantiles of the null distribution can be estimated using the sample quantiles available in statistical software such as R, and these quantiles can be utilized for decision-making purposes. The details of the sample quantile computation can be found in Hyndman and Fan (1996). For instance, if \hat{D} is greater than or equal to the 95% sample quantile, denoted as $Q_{null}(0.95)$, we can conclude that the estimated distance for the true residual plot is significantly different from the estimated distance for null plots with a 95% significance level. Based on our experience, to obtain a stable estimate of the 95% quantile, the number of null plots, n_{null} , typically needs to be at least 100. However, if the null distribution exhibits a long tail, a larger number of null plots may be required. Alternatively, a p -value can be used to represent the probability of observing an event equally or more extreme than the given event under the null hypothesis H_0 , and it can be estimated by $\frac{1}{m} \sum_{i=1}^{m-1} I(\hat{D}_{null}^{(i)} \geq \hat{D})$.

If precision in sample quantiles is not the main priority, using a pre-calculated table

of quantiles is an available option. Such a table offers pre-determined quantiles for a specified number of observations. It is generated by assessing numerous null plots derived from various simulated regression models and averaging them. Essentially, this shifts the computational burden from the user to the developer.

6.2. *Bootstrapping*

Bootstrap is often employed in linear regression when conducting inference for estimated parameters. It is typically done by sampling individual cases with replacement and refitting the regression model. If the observed data accurately reflects the true distribution of the population, the bootstrapped estimates can be used to measure the variability of the parameter estimate without making strong distributional assumptions about the data generating process.

Similarly, bootstrap can be applied on the estimated distance \hat{D} . For each refitted model $M_{boot}^{(i)}$, there will be an associated residual plot $V_{boot}^{(i)}$ which can be fed into the computer vision model to obtain $\hat{D}_{boot}^{(i)}$, where $i = 1, \dots, n_{boot}$, and n_{boot} is the number of bootstrapped samples. If we are interested in the variation of \hat{D} , we can use $\hat{D}_{boot}^{(i)}$ to estimate a confidence interval.

Alternatively, since each $M_{boot}^{(i)}$ has a set of estimated coefficients $\hat{\beta}_{boot}^{(i)}$ and an estimated variance $\hat{\sigma}_{boot}^{(i)}$, a new approximated null distribution can be construed and the corresponding 95% sample quantile $Q_{boot}^{(i)}(0.95)$ can be computed. Then, if $\hat{D}_{boot}^{(i)} \geq Q_{boot}^{(i)}(0.95)$, H_0 will be rejected for $M_{boot}^{(i)}$. The ratio of rejected $M_{boot}^{(i)}$ among all the refitted models provides an indication of how often the assumed regression model are considered to be incorrect if the data can be obtained repetitively from the same data generating process. But this approach is computationally very expensive because it requires $n_{boot} \times n_{null}$ times of residual plot assessment. In practice, $Q_{null}(0.95)$ can be used to replace $Q_{boot}^{(i)}(0.95)$ in the computation.

7. Data Generation

7.1. Simulation Scheme

While observational data is frequently employed in training models for real-world applications, the data generating process of observational data often remains unknown, making computation for our target variable D unattainable. Consequently, the computer vision models developed in this study were trained using synthetic data, including 80000 training images and 8000 test images. This approach provided us with precise label annotations. Additionally, it ensured a large and diverse training dataset, as we had control over the data generating process, and the simulation of the training data was relatively cost-effective.

We have incorporated three types of residual departures of linear regression model in the training data, including non-linearity, heteroskedasticity and non-normality. All three departures can be summarised by the data generating process formulated as

$$\mathbf{y} = \mathbf{1}_n + \mathbf{x}_1 + \beta_1 \mathbf{x}_2 + \beta_2 (\mathbf{z} + \beta_1 \mathbf{w}) + \mathbf{k} \odot \boldsymbol{\varepsilon}, \quad (8)$$

$$\mathbf{z} = \text{He}_j(g(\mathbf{x}_1, 2)), \quad (9)$$

$$\mathbf{w} = \text{He}_j(g(\mathbf{x}_2, 2)), \quad (10)$$

$$\mathbf{k} = \sqrt{\mathbf{1}_n + b(2 - |a|)(\mathbf{x}_1 + \beta_1 \mathbf{x}_2 - a \mathbf{1}_n)^2}, \quad (11)$$

where \mathbf{y} , \mathbf{x}_1 , \mathbf{x}_2 , \mathbf{z} , \mathbf{w} , \mathbf{k} and $\boldsymbol{\varepsilon}$ are vectors of size n , $\mathbf{1}_n$ is a vector of ones of size n , \mathbf{x}_1 and \mathbf{x}_2 are two independent predictors, $\text{He}_j(\cdot)$ is the j th-order probabilist's Hermite polynomials (Hermite 1864), the $\sqrt{(\cdot)}$ and $(\cdot)^2$ operators are element-wise operators, \odot is the Hadamard product, and $g(\mathbf{x}, k)$ is a scaling function to enforce the support of the random vector to be $[-k, k]^n$ defined as

$$g(\mathbf{x}, k) = 2k \cdot \frac{\mathbf{x} - x_{min} \mathbf{1}_n}{x_{max} - x_{min}} - k \mathbf{1}_n, \text{ for } k > 0,$$

Table 2. Factors used in the data generating process for synthetic data simulation. Factor j and a controls the non-linearity shape and the heteroskedasticity shape respectively. Factor b , σ_ε and n control the signal strength. Factor dist_ε , dist_{x1} and dist_{x2} specifies the distribution of ε , X_1 and X_2 respectively.

Factor	Domain
j	$\{2, 3, \dots, 18\}$
a	$[-1, 1]$
b	$[0, 100]$
β_1	$\{0, 1\}$
β_2	$\{0, 1\}$
dist_ε	{discrete, uniform, normal, lognormal}
dist_{x1}	{discrete, uniform, normal, lognormal}
dist_{x2}	{discrete, uniform, normal, lognormal}
σ_ε	$[0.0625, 9]$
σ_{X1}	$[0.3, 0.6]$
σ_{X2}	$[0.3, 0.6]$
n	$[50, 500]$

where $x_{min} = \min_{i \in \{1, \dots, n\}} x_i$, $x_{max} = \max_{i \in \{1, \dots, n\}} x_i$ and x_i is the i -th entry of \mathbf{x} .

The residuals and fitted values of the fitted model were obtained by regressing \mathbf{y} on \mathbf{x}_1 . If $\beta_1 \neq 0$, \mathbf{x}_2 was also included in the design matrix. This data generation process was adapted from Li et al. (2023), where it was utilized to simulate residual plots exhibiting non-linearity and heteroskedasticity visual patterns for human subject experiments. A summary of the factors utilized in Equation 8 is provided in Table 2.

In Equation 8, \mathbf{z} and \mathbf{w} represent higher-order terms of \mathbf{x}_1 and \mathbf{x}_2 , respectively. If $\beta_2 \neq 0$, the regression model will encounter non-linearity issues. Parameter j serves as a shape parameter that controls the number of tuning points in the non-linear pattern. Typically, higher values of j lead to an increase in the number of tuning points, as illustrated in Figure 4.

Additionally, Scaling factor \mathbf{k} directly affects the error distribution and it is correlated with \mathbf{x}_1 and \mathbf{x}_2 . If $b \neq 0$ and $\varepsilon \sim N(\mathbf{0}_n, \sigma^2 \mathbf{I}_n)$, the constant variance assumption will be violated. Parameter a is a shape parameter controlling the location of the smallest variance in a residual plot as shown in Figure 5.

Non-normality violations arise from specifying a non-normal distribution for ε . In the synthetic data simulation, four distinct error distributions are considered, including discrete, uniform, normal, and lognormal distributions, as presented in Figure 6.

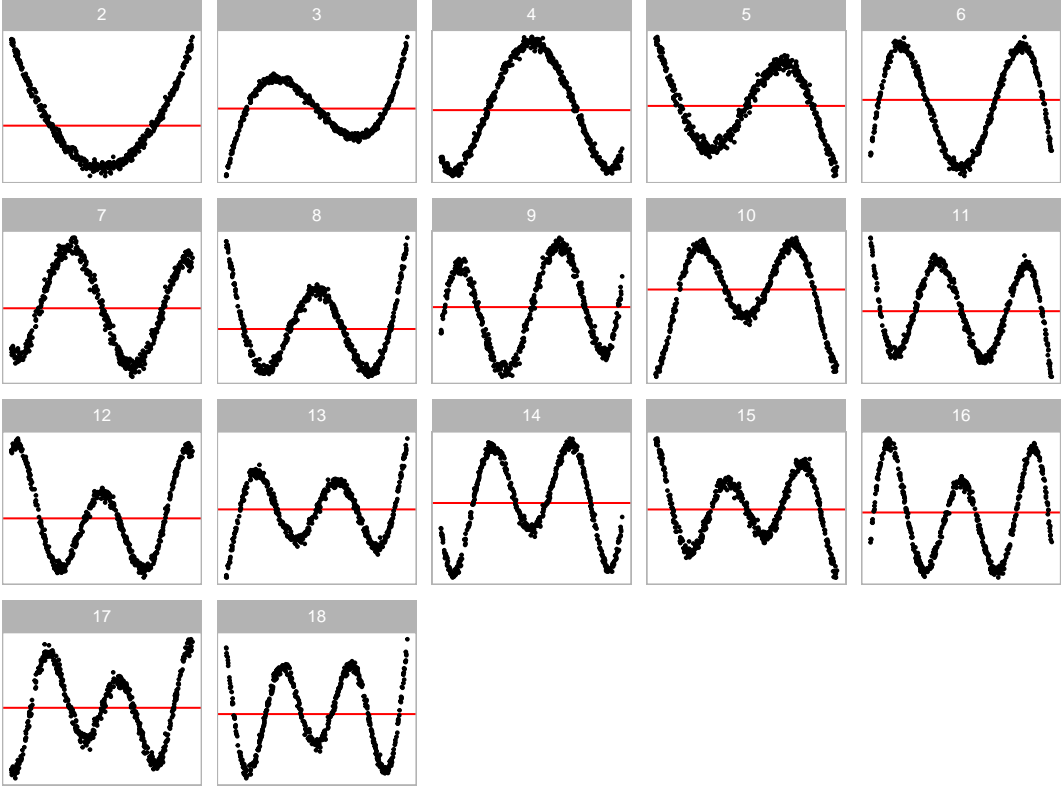


Figure 4. Non-linearity forms generated for the synthetic data simulation. The 17 shapes are generated by varying the order of polynomial given by j in $He_j(\cdot)$.

Each distribution imparts unique characteristics to the residuals. The discrete error distribution introduces discreteness in residuals, while the lognormal distribution typically yields outliers. Uniform error distribution may result in residuals filling the entire space of the residual plot. All of these distributions exhibit visual distinctions from the normal error distribution.

Equation 8 accommodates the incorporation of the second predictor \mathbf{x}_2 . Introducing it into the data generation process by setting $\beta_1 = 1$ significantly enhances the complexity of the shapes, as illustrated in Figure 7. In comparison to Figure 4, Figure 7 demonstrates that the non-linear shape resembles a surface rather than a single curve. This augmentation can facilitate the computer vision model in learning visual patterns from residual plots of the multiple linear regression model.

In real-world analysis, it's not uncommon to encounter instances where multiple model violations coexist. In such cases, the residual plots often exhibit a mixed pattern of visual anomalies corresponding to different types of model violations. Figure 8 and

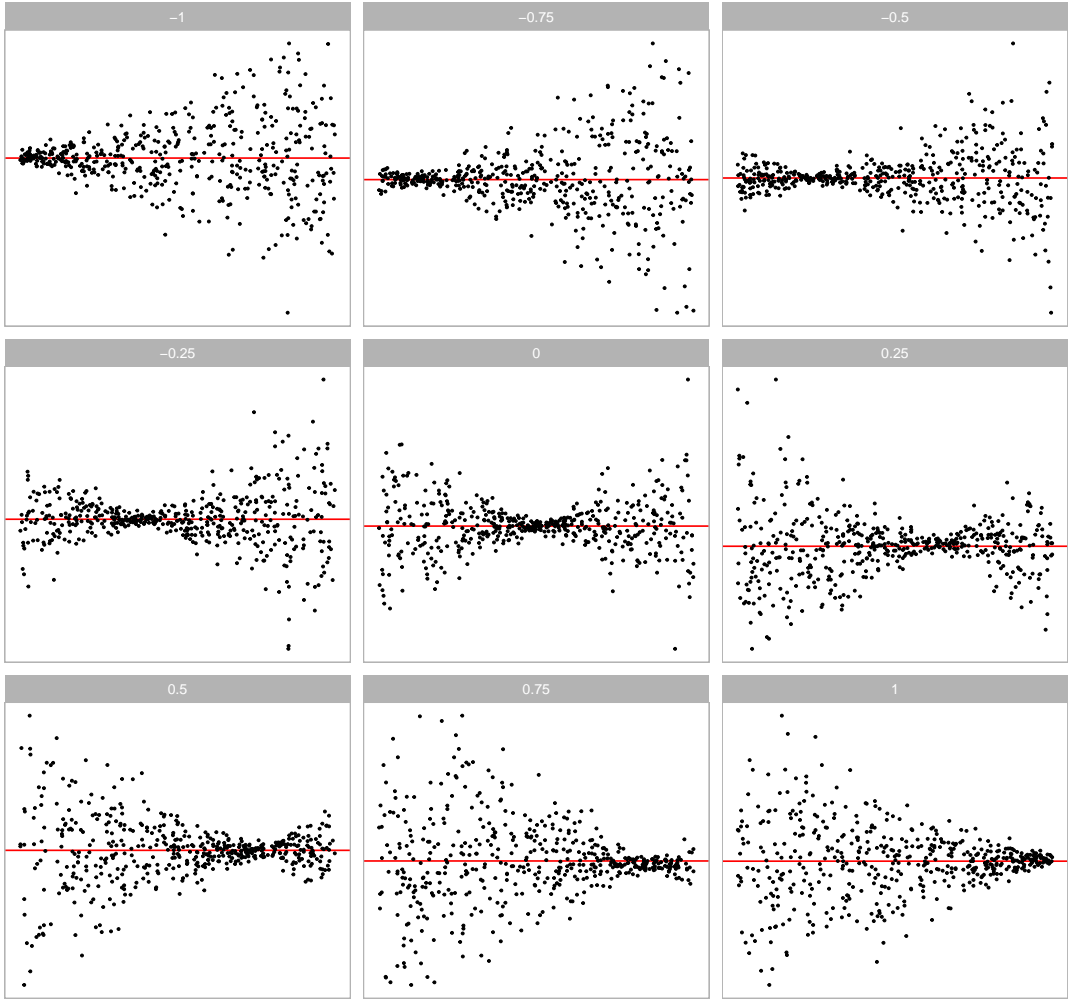


Figure 5. Heteroskedasticity forms generated for the synthetic data simulation. Different shapes are controlled by the continuous factor a between -1 and 1. For $a = -1$, the residual plot exhibits a "left-triangle" shape. And for $a = 1$, the residual plot exhibits a "right-triangle" shape.

9 show the visual patterns of models with multiple model violations.

7.2. Scagnostics

In Section 1, we mentioned that scagnostics consist of a set of manually designed visual feature extraction functions. While our computer vision model will learn its own feature extraction function during training, leveraging additional information from scagnostics can enhance the model's predictive accuracy.

For each generated residual plot, we computed four scagnostics – “Monotonic”, “Sparse”, “Splines”, and “Striped” – using the `cassowaryr` R package (Mason et al. 2022). These computed measures, along with the number of observations from the

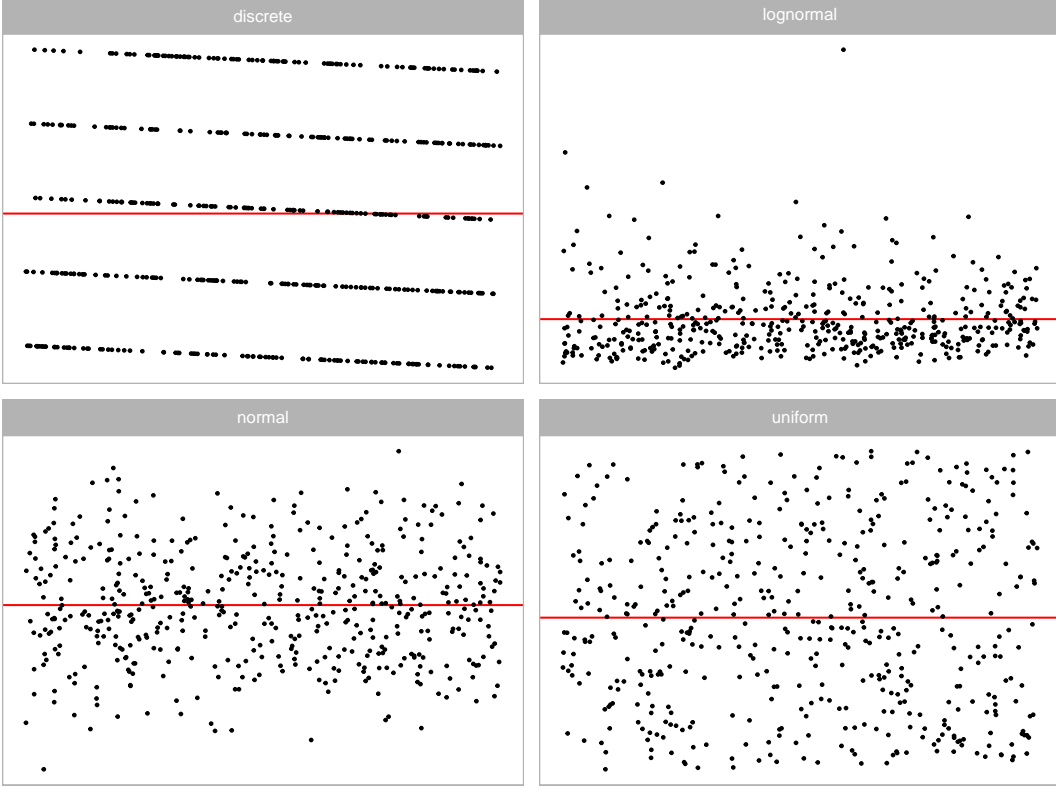


Figure 6. Non-normality forms generated for the synthetic data simulation. Four different error distributions including discrete, lognormal, normal and uniform are considered.

fitted model, were provided as the second input for the computer vision model. While other scagnostics provide valuable insights, they come with high computational costs and are not suitable for quick inference.

7.3. *Balanced Dataset*

To train a robust computer vision model, we deliberately controlled the distribution of the target variable D in the training data. We ensured that it followed a uniform distribution between 0 and 7. This was achieved by organizing 50 buckets, each exclusively accepting training samples with D falling within the range $[7(i - 1)/49, 7i/49]$ for $i < 50$, where i represents the index of the i -th bucket. For the 50-th bucket, any training samples with $D \geq 7$ were accepted.

With 80000 training images prepared, each bucket accommodated a maximum of $80000 \div 50 = 1600$ training samples. The simulator iteratively sampled parameter values from the parameter space, generated residuals and fitted values using the data

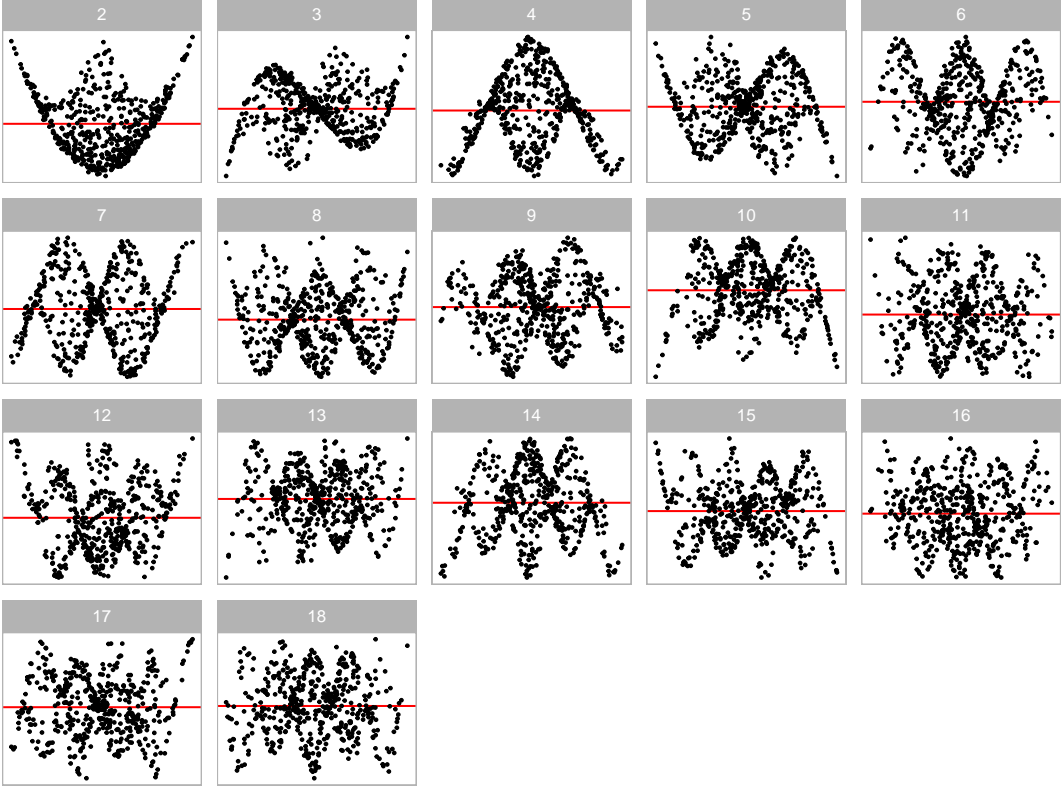


Figure 7. Residual plots of multiple linear regression models with non-linearity issues. The 17 shapes are generated by varying the order of polynomial given by j in $He_j(\cdot)$. A second predictor α_2 is introduced to the regression model to create complex shapes.

generation process, computed the distance, and checked if the sample fitted within the corresponding bucket. This process continued until all buckets were filled.

Similarly, we adopted the same methodology to prepare 8000 test images for performance evaluation and model diagnostics.

8. Model Architecture

The architecture of the computer vision model is adapted from a well-established architecture known as VGG16, which has demonstrated high performance in image classification (Simonyan and Zisserman 2014). Figure 10 provides a diagram of the architecture. More details about the neural network layers used in this study are provided in the Appendix.

The model begins with an input layer of shape $n \times h \times w \times 3$, capable of handling n RGB images. This is followed by a grayscale conversion layer utilizing the luma

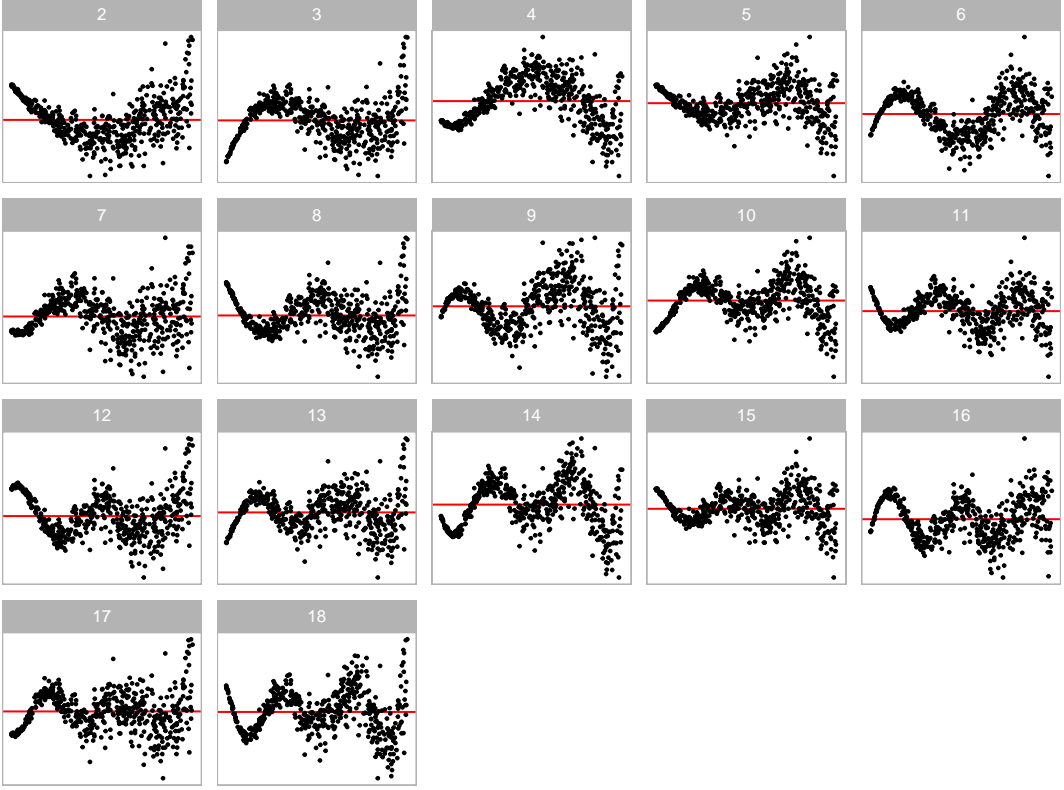


Figure 8. Residual plots of models violating both the non-linearity and the heteroskedasticity assumptions. The 17 shapes are generated by varying the order of polynomial given by j in $He_j(\cdot)$, and the "left-triangle" shape is introduced by setting $a = -1$.

formula under the Rec. 601 standard, which converts the colour image to grayscale. Grayscale suffices for our task since data points are plotted in black. We experiment with three combinations of h and w : 32×32 , 64×64 , and 128×128 , aiming to achieve sufficiently high image resolution for the problem at hand.

The processed image is used as the input for the first convolutional block. The model comprises at most five consecutive convolutional blocks, mirroring the original VGG16 architecture. Within each block, there are two 2D convolutional layers followed by two activation layers, respectively. Subsequently, a 2D max-pooling layer follows the second activation layer. The 2D convolutional layer convolves the input with a fixed number of 3×3 convolution filters, while the 2D max-pooling layer downsamples the input along its spatial dimensions by taking the maximum value over a 2×2 window for each channel of the input. The activation layer employs the rectified linear unit (ReLU) activation function, a standard practice in deep learning, which introduces a non-linear transformation of the output of the 2D convolutional layer. Additionally, to

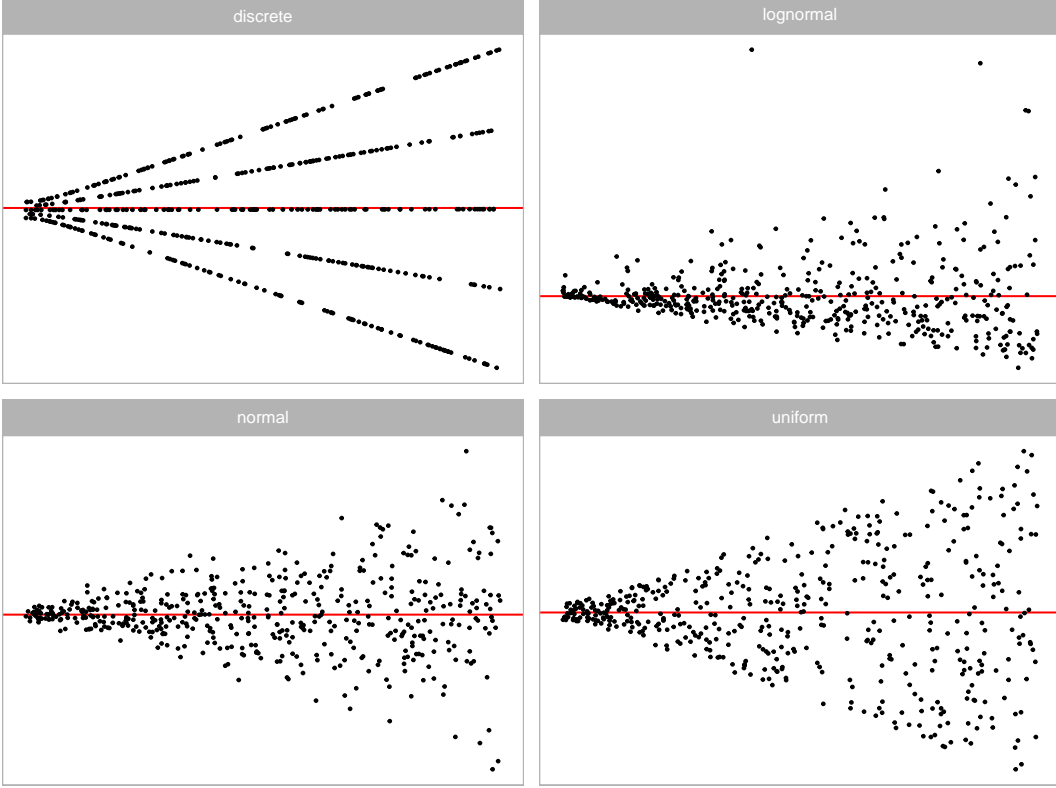


Figure 9. Residual plots of models violating both the non-normality and the heteroskedasticity assumptions. The four shapes are generated by using four different error distributions including discrete, lognormal, normal and uniform, and the "left-triangle" shape is introduced by setting $a = -1$.

regularize training, a batch normalization layer is added after each 2D convolutional layer and before the activation layer. Finally, a dropout layer is appended at the end of each convolutional block to randomly set some inputs to zero during training, further aiding in regularization.

The output of the last convolutional block is summarized by either a global max pooling layer or a global average pooling layer, resulting in a two-dimensional tensor. To leverage the information contained in scagnostics, this tensor is concatenated with an additional $n \times 5$ tensor, which contains the "Monotonic," "Sparse," "Splines," and "Striped" measures, along with the number of observations for n residual plots.

The concatenated tensor is then fed into the final prediction block. This block consists of two fully-connected layers. The first layer contains at least 128 units, followed by a dropout layer. Occasionally, a batch normalization layer is inserted between the fully-connected layer and the dropout layer for regularization purposes. The second fully-connected layer consists of only one unit, serving as the output of the model.

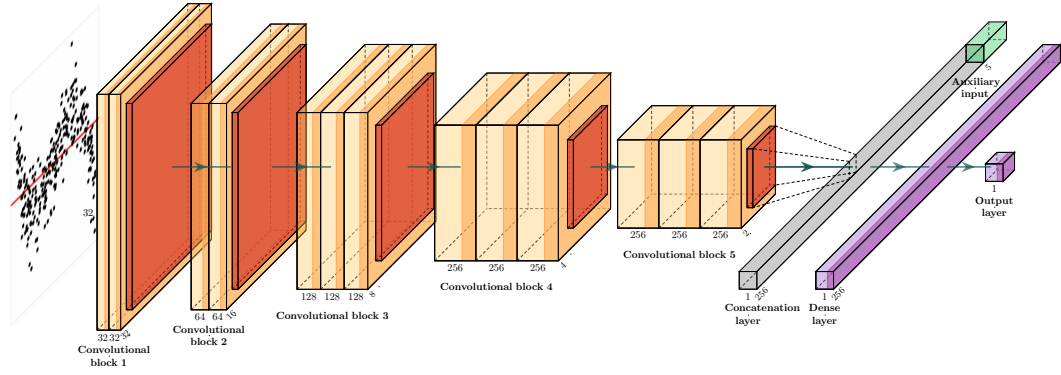


Figure 10. Diagram of the architecture of the optimized computer vision model. Numbers at the bottom of each box show the shape of the output of each layer. The band of each box drawn in a darker colour indicates the use of the rectified linear unit activation function. Yellow boxes are 2D convolutional layers, orange boxes are pooling layers, the grey box is the concatenation layer, and the purple boxes are dense layers.

The model weights θ were randomly initialized and they were optimized by the Adam optimizer with the mean square error loss function

$$\hat{\theta} = \underset{\theta}{\operatorname{argmin}} \frac{1}{n_{train}} \sum_{i=1}^{n_{train}} (D_i - f_{\theta}(V_i, S_i))^2,$$

where n_{train} is the number of training samples, V_i is the i -th residual plot and S_i is the additional information about the i -th residual plot including four scagnostics and the number of observations.

9. Model Training

To achieve a near-optimal deep learning model, hyperparameters like the learning rate often need to be fine-tuned using a tuner. In our study, we utilized the Bayesian optimization tuner from the `KerasTuner` Python library (O’Malley et al. 2019) for this purpose. A comprehensive list of hyperparameters is provided in Table 3.

The “number of base filters” determines the number of filters for the first 2D convolutional layer. In the VGG16 architecture, the number of filters for the 2D convolutional layer in a block is typically twice the number in the previous block, except for the last block, which maintains the same number of convolution filters as the pre-

vious one. This hyperparameter aids in controlling the complexity of the computer vision model. Higher numbers of base filters result in more trainable parameters. Likewise, the “number of units for the fully-connected layer” determines the complexity of the final prediction block. Increasing the number of units enhances model complexity, resulting in more trainable parameters.

The dropout rate and batch normalization are flexible hyperparameters that work in conjunction with other parameters to facilitate smooth training. A higher dropout rate is necessary when the model tends to overfit the training dataset by learning too much noise. Conversely, a lower dropout rate is preferred when the model is complex and challenging to converge. Batch normalization, on the other hand, addresses the internal covariate shift problem arising from the randomness in weight initialization and input data. It helps stabilize and accelerate the training process by normalizing the activations of each layer.

Additionally, incorporating additional inputs such as scagnostics and the number of observations can potentially enhance prediction accuracy. Therefore, we allowed the tuner to determine whether these inputs were necessary for optimal model performance.

The learning rate is a crucial hyperparameter, as it dictates the step size of the optimization algorithm. A high learning rate can help the model avoid local minima but risks overshooting and missing the global minimum. Conversely, a low learning rate smoothens the training process but makes the convergence time longer and increases the likelihood of getting trapped in local minima.

Our model was trained on the MASSIVE M3 high-performance computing platform (Goscinski et al. 2014), using TensorFlow (Abadi et al. 2016) and Keras (Chollet et al. 2015). During training, 80% of the training data was utilized for actual training, while the remaining 20% was used as validation data. The Bayesian optimization tuner conducted 100 trials to identify the best hyperparameter values based on validation root mean square error. The tuner then restored the best epoch of the best model from the trials. Additionally, we applied early stopping, terminating the training process if the validation root mean square error fails to improve for 50 epochs. The maximum allowed epochs was set at 2000, although no models reached this threshold.

Table 3. Name of hyperparameters and their corresponding domain for the computer vision model.

Hyperparameter	Domain
Number of base filters	{4, 8, 16, 32, 64}
Dropout rate for convolutional blocks	[0.1, 0.6]
Batch normalization for convolutional blocks	{false, true}
Type of global pooling	{max, average}
Ignore additional inputs	{false, true}
Number of units for the fully-connected layer	{128, 256, 512, 1024, 2048}
Batch normalization for the fully-connected layer	{false, true}
Dropout rate for the fully-connected layer	[0.1, 0.6]
Learning rate	[1e-8, 1e-1]

Table 4. Hyperparameters values for the optimized computer vision models with different input sizes.

Hyperparameter	32 × 32	64 × 64	128 × 128
Number of base filters	32	64	64
Dropout rate for convolutional blocks	0.4	0.3	0.4
Batch normalization for convolutional blocks	true	true	true
Type of global pooling	max	average	average
Ignore additional inputs	false	false	false
Number of units for the fully-connected layer	256	256	256
Batch normalization for the fully-connected layer	false	true	true
Dropout rate for the fully-connected layer	0.2	0.4	0.1
Learning rate	0.0003	0.0006	0.0052

Based on the tuning process described above, the optimized hyperparameter values are presented in Table 4. It was observable that a minimum of 32 base filters was necessary, with the preferable choice being 64 base filters for both the 64×64 and 128×128 models, mirroring the original VGG16 architecture. The optimized dropout rate for convolutional blocks hovered around 0.4, and incorporating batch normalization for convolutional blocks proved beneficial for performance.

All optimized models chose to retain the additional inputs, contributing to the reduction of validation error. The number of units required for the fully-connected layer was 256, a relatively modest number compared to the VGG16 classifier, suggesting that the problem at hand was less complex. The optimized learning rates were smaller than the default value recommended by Keras, which is 0.001.

10. Results

10.1. Model Performance

The training and test performance for the optimized models with three different input sizes are summarized in Table 5. Among these models, the 64×64 model and the 32×32 model consistently exhibited the best training and test performance, respectively. The mean absolute error indicated that the difference between \hat{D} and D was approximately 0.43 on the test set, a negligible deviation considering the normal range of D typically falls between 0 and 7. The high R^2 values also suggested that the predictions were largely linearly correlated with the target.

Figure 11 presents a hexagonal heatmap for $D - \hat{D}$ versus \hat{D} . The red smoothing curves, fitted by generalized additive models (Hastie 2017), demonstrate that all the optimized models perform admirably on both the training and test sets. No structural issues are noticeable in Figure 11, but some minor issues regarding over-prediction and under-prediction are observed.

The figure highlights that most under-predictions occurred when $\hat{D} < 3$, while over-predictions occurred predominantly when $3 < \hat{D} < 6$. For input images representing null plots, it was expected that the models will over-predict the distance, as explained in Section 6.1. However, it can not explain the under-prediction issue. Therefore, we analysed the relationship between residuals and all the factors involved in the data generating process. We found that most issues actually arose from non-linearity problems and the presence of a second predictor in the regression model as illustrated in Figure 12. When the variance for the error distribution was small, the optimized model tended to under-predict the distance. Conversely, when the error distribution had a large variance, the model tended to over-predict the distance.

Since most of the deviation stemmed from the presence of non-linearity violations, to further investigate this, we split the test set based on violation types and re-evaluated the performance, as detailed in Table 6. It was evident that metrics for null plots were notably worse compared to other categories. Furthermore, residual plots solely exhibiting non-normality issues were the easiest to predict, with very low test root mean square error (RMSE) at around 0.3. Residual plots with non-linearity issues

Table 5. The training and test performance of three optimized models with different input sizes.

	RMSE	R^2	MAE	Huber loss
Training set				
32 × 32	0.531	0.937	0.364	0.126
64 × 64	0.405	0.963	0.260	0.072
128 × 128	0.432	0.959	0.290	0.084
Test set				
32 × 32	0.660	0.901	0.434	0.181
64 × 64	0.674	0.897	0.438	0.186
128 × 128	0.692	0.892	0.460	0.199

Table 6. The training and test performance of the 32×32 model presented with different model violations.

Violations	#training samples	Training RMSE	#test samples	Test RMSE
no violations	1546	1.149	155	1.267
non-linearity	22184	0.625	2218	0.787
heteroskedasticity	10826	0.528	1067	0.602
non-linearity + heteroskedasticity	10221	0.593	985	0.751
non-normality	10797	0.279	1111	0.320
non-linearity + non-normality	8835	0.472	928	0.600
heteroskedasticity + non-normality	7870	0.354	819	0.489
non-linearity + heteroskedasticity + non-normality	7721	0.432	717	0.620

were more challenging to assess than those with heteroskedasticity or non-normality issues. Assessing residual plots with heteroskedasticity was not as difficult as assessing those with non-linearity issues. When multiple violations were introduced to a residual plot, the performance metrics typically lay between the metrics for each individual violation.

Based on the model performance metrics, we chose to use the best-performing model evaluated on the test set, namely the 32×32 model, for the subsequent analysis.

10.2. Comparison with Human Visual Inference and Conventional Tests

10.2.1. Overview of the Human Subject experiment

In order to check the validity of the proposed computer vision model, residual plots presented in the human subject experiment conducted by Li et al. (2023) will be assessed.

This study has collected 7974 human responses to 1152 lineups. Each lineup contains

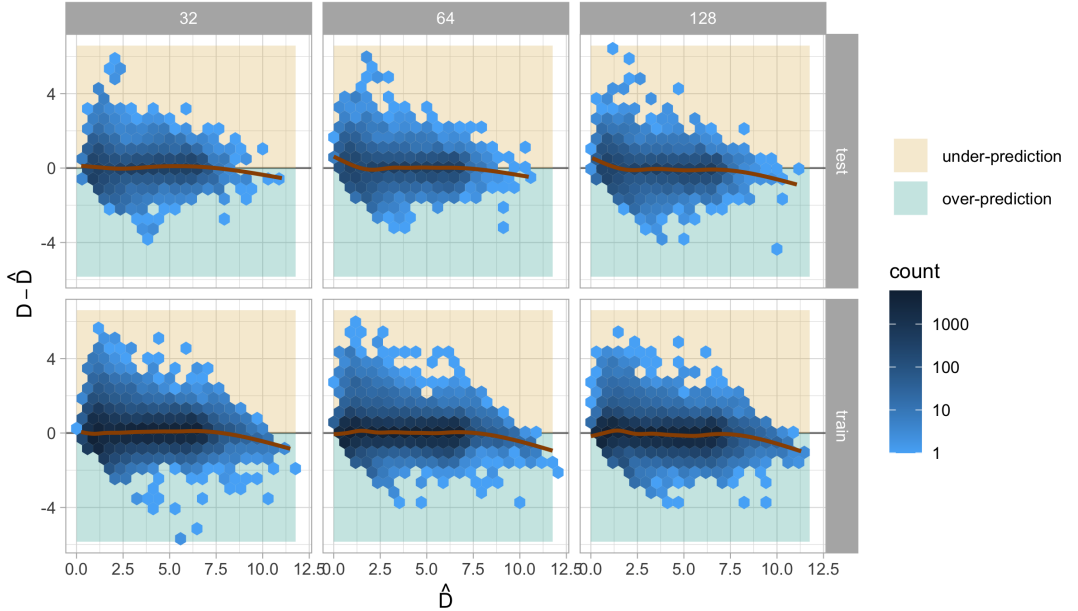


Figure 11. Hexagonal heatmap for residuals vs predicted distance on training and test data for three optimized models with different input sizes. The brown lines are smoothing curves produced by fitting generalized additive models. The area over the zero line in light yellow indicates under-prediction, and the area under the zero line in light green indicates over-prediction.

one randomly placed true residual plot and 19 null plots. Among the 1152 lineups, 24 are attention check lineups in which the visual patterns are designed to be extremely obvious and very different from the corresponding to null plots, 36 are null lineups where all the lineups consist of only null plots, 279 are lineups with uniform predictor distribution evaluated by 11 participants, and the remaining 813 are lineups with discrete, skewed or normal predictor distribution evaluated by 5 participants. Attention check lineups and null lineups will not be assessed in the following analysis.

In Li et al. (2023), the residual plots are simulated from a data generating process which is a special case of Equation 8. The main characteristic is the model violations are introduced separately, meaning non-linearity and heteroskedasticity will not co-exist in one lineup but assigned uniformly to all lineups. Additionally, non-normality and multiple predictors are not considered in the experimental design.

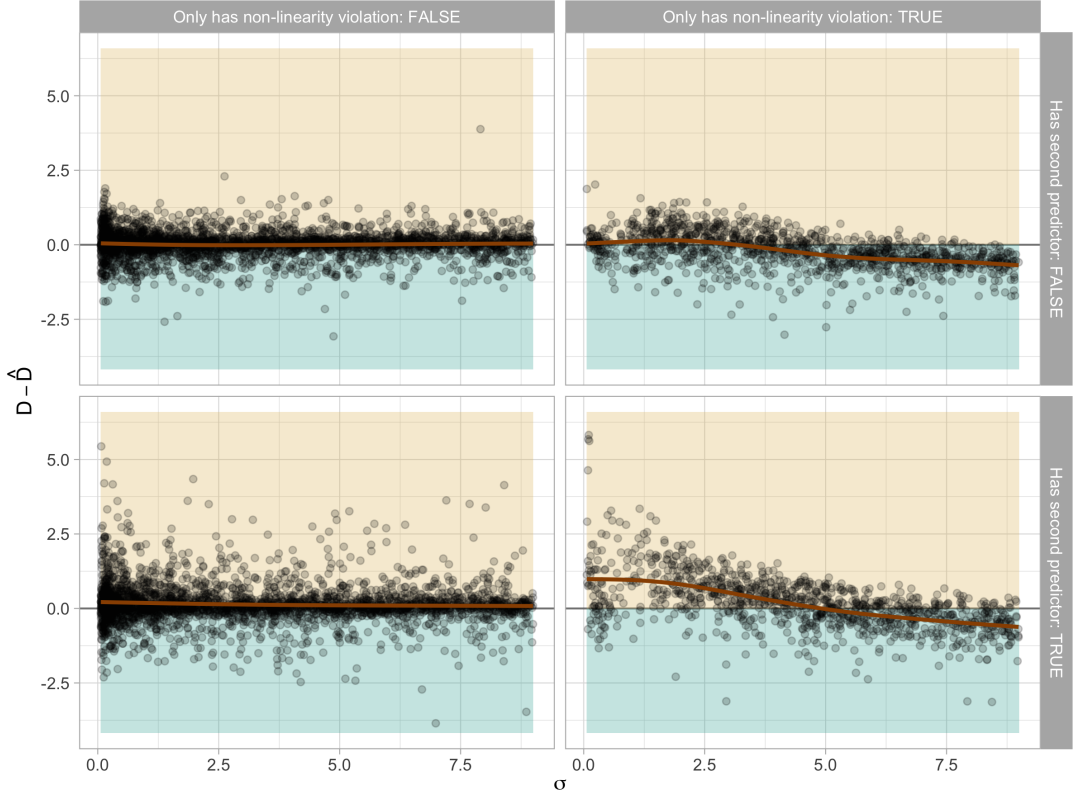


Figure 12. Scatter plots for residuals vs σ on test data for the 32×32 optimized model. The data is grouped by whether the regression has only non-linearity violation, and whether it includes a second predictor in the regression formula. The brown lines are smoothing curves produced by fitting generalized additive models. The area over the zero line in light yellow indicates under-prediction, and the area under the zero line in light green indicates over-prediction.

10.2.2. Model performance on the human data

For each lineup used in Li et al. (2023), there is one true residual plot and 19 null plots. While the distance D for the true residual plot depends on the underlying data generating process, the distance D for the null plots is zero. We have used our optimized computer vision model to estimate distance for both the true residual plots and the null plots. To have a fair comparison, H_0 will be rejected if the true residual plot has the greatest approximated distance among all plots in a lineup. Additionally,

Table 7. The performance of the 32×32 model on the data used in the human subject experiment.

Violation	RMSE	R^2	MAE	Huber loss
heteroskedasticity	0.721	0.852	0.553	0.235
non-linearity	0.738	0.770	0.566	0.246

the appropriate conventional tests including the Ramsey Regression Equation Specification Error Test (RESET) (Ramsey 1969) for non-linearity and the Breusch-Pagan test (Breusch and Pagan 1979) for heteroskedasticity were applied on the same data for comparison.

The performance metrics of \hat{D} for true residual plots are outlined in Table 7. It's notable that all performance metrics are slightly worse than those evaluated on the test data. Nevertheless, the mean absolute error remains at a low level, and the linear correlation between the prediction and the true value remains very high. Lineups with non-linearity issues are more challenging to predict than those with heteroskedasticity issues.

Table 8 provides a summary of the agreement between decisions made by the computer vision model and conventional tests. The agreement rates between conventional tests and the computer vision model are 85.95% and 79.69% for residual plots containing heteroskedasticity and non-linearity patterns, respectively. These figures are higher than those calculated for visual tests conducted by human, indicating that the computer vision model exhibits behaviour more akin to the best available conventional tests. However, Figure 13 shows that the computer vision model does not always reject when the conventional tests reject. And a small number of plots will be rejected by computer vision model but not by conventional tests. This suggests that conventional tests are more sensitive than the computer vision model.

Figure 15 further illustrates the decisions made by visual tests conducted by human, computer vision models, and conventional tests, using a parallel coordinate plots. It can be observed that all three tests will agree with each other for around 50% of the cases. When visual tests conducted by human do not reject, there are substantial amount of cases where computer vision model also not reject but conventional tests reject. There are much fewer cases that do not reject by visual tests and conventional tests, but reject by computer vision models. This indicates computer vision model can behave like visual tests conducted by human better than conventional tests. Moreover, there are great proportion of cases where visual tests conducted by human is the only test who does not reject, .

When plotting the decision against the distance, as illustrated in Figure 14, several

observations emerge. Firstly, for the computer vision model, when the distance $D > 4$, almost all residual plots are rejected. However, for visual tests conducted by humans, the threshold is higher, set at $D > 5$. And conventional tests exhibit some non-rejection cases for $D > 3$. Moreover, the computer vision model tends to have fewer rejected cases than conventional tests when $D < 2$. However, visual tests demonstrate the lowest sensitivity to residual plots with small distances. Therefore, tests based on the computer vision model are less sensitive to small deviations from model assumptions than conventional tests but more sensitive to moderate deviations. Rejection decisions are fitted by logistic regression models with no intercept terms but an offset equals to $\log(0.05/0.95)$. The fitting curves for the computer vision model fall between those of conventional tests and visual tests for both non-linearity and heteroskedasticity. There is still potential to refine the computer vision model to better align its behaviour with visual tests.

In the experiment conducted in Li et al. (2023), participants were allowed to make multiple selections for a lineup. The weighted detection rate is computed by assigning weights to each detection. If the participant selects zero plots, the corresponding weight is 0.05; otherwise, the weight is 1 divided by the number of selections. The δ -difference is defined by Chowdhury et al. (2018) as

$$\delta = \hat{D} - \max_j \left(\hat{D}_{null}^{(j)} \right) \quad \text{for } j = 1, \dots, m - 1, \quad (12)$$

where $\hat{D}_{null}^{(j)}$ is the approximated distance for the j -th null plot, and m is the number of plots in a lineup.

Figure 16 displays the scatter plot of the weighted detection rate vs the δ -difference. It indicates that the weighted detection rate increases as the δ -difference increases, particularly when the δ -difference is greater than zero. A negative δ -difference suggests that there is at least one null plot in the lineup with a stronger visual signal than the true residual plot. In some instances, the weighted detection rate is close to one, yet the δ -difference is negative. This discrepancy implies that the distance measure, or the estimated distance, may not perfectly reflect actual human behaviour.

Table 8. Summary of the comparison of decisions made by computer vision model with decisions made by conventional tests and visual tests conducted by human.

Violations	#Samples	#Agreements	Agreement rate
Compared with conventional tests			
heteroskedasticity	540	464	0.8593
non-linearity	576	459	0.7969
Compared with visual tests conducted by human			
heteroskedasticity	540	367	0.6796
non-linearity	576	385	0.6684

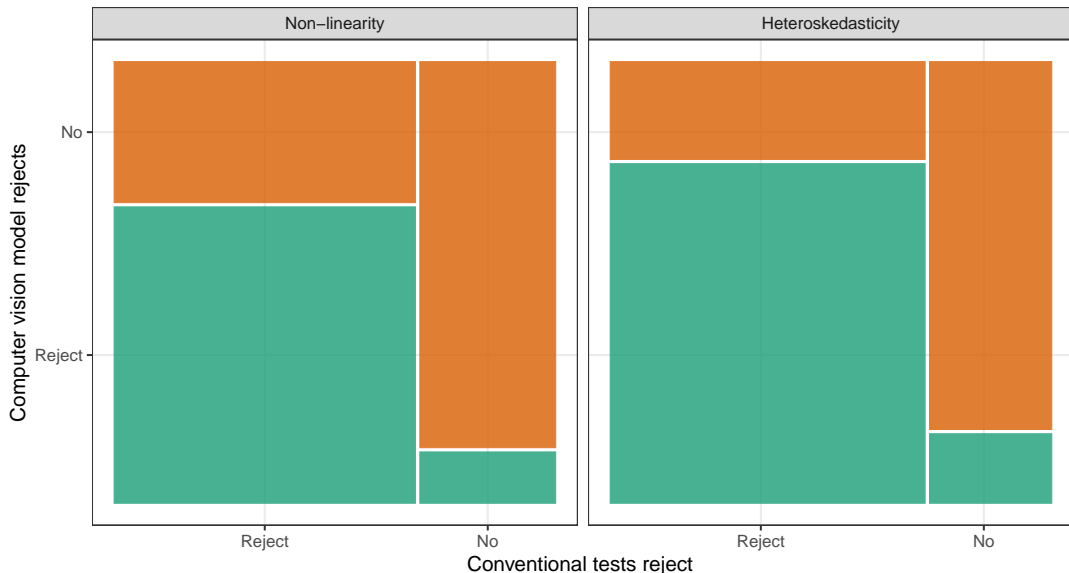


Figure 13. Rejection rate ($p\text{-value} \leq 0.05$) of computer vision models conditional on conventional tests on non-linearity (left) and heteroskedasticity (right) lineups displayed using a mosaic plot.

11. Examples

In this section, we will present the performance of trained computer vision model on three example datasets. These include the dataset associated with the residual plot displaying a “left-triangle” shape, as displayed in Figure 1, along with the Boston housing dataset, and the “dino” datasets from the `datasaurus` R package.

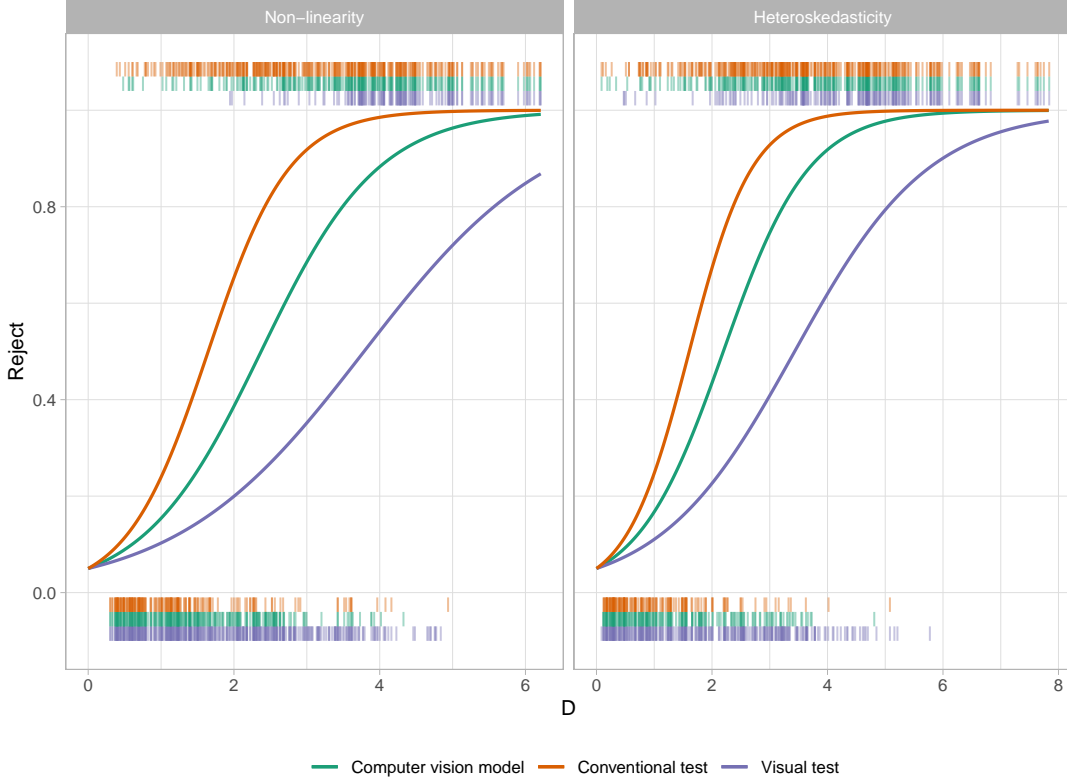


Figure 14. Comparison of power of visual tests, conventional tests and the computer vision model. Marks along the x-axis at the bottom of the plot represent rejections made by each type of test. Marks at the top of the plot represent acceptances. Power curves are fitted by logistic regression models with no intercept but an offset equals to $\log(0.05/0.95)$.

The first example illustrates a scenario where both the computer vision model and human visual inspection successfully avoid rejecting H_0 when H_0 is true, contrary to conventional tests. This underscores the necessity of visually examining the residual plot.

In the second example, we encounter a more pronounced violation of the model, resulting in rejection of H_0 by all three tests. This highlights the practicality of the computer vision model, particularly for less intricate tasks.

The third example presents a situation where the model deviation is non-typical. Here, the computer vision model and human visual inspection reject H_0 , whereas some commonly used conventional tests do not. This emphasizes the benefits of visual inspection and the unique advantage of the computer vision model, which, like humans, makes decisions based on visual discoveries.

Additionally, we will outline the workflow for employing this model with the `autovi`

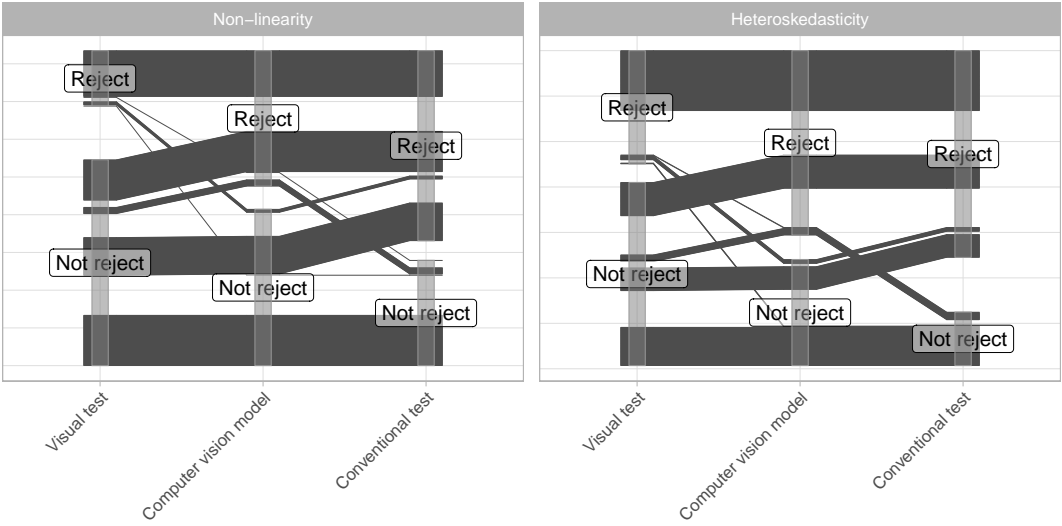


Figure 15. Parallel coordinate plots of decisions made by computer vision model, conventional tests and visual tests made by human.

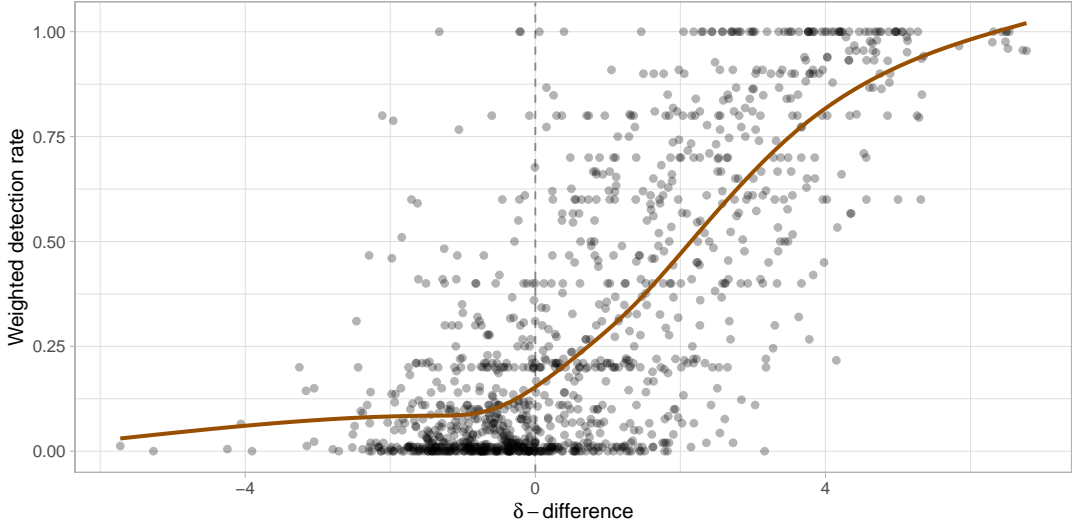


Figure 16. A weighted detection rate vs δ -differnce plot. The brown line is smoothing curve produced by fitting generalized additive models

R package.

11.1. *Left-triangle*

In Section 1, we presented an example residual plot showcased in Figure 1, illustrating how humans might misinterpret the “left-triangle” shape as indicative of heteroskedasticity. Additionally, the Breusch-Pagan test yielded a rejection with a p -value of 0.046, despite the residuals originating from a correctly specified model. Figure 18 offers a

lineup for this fitted model, showcasing various degrees of “left-triangle” shape across all residual plots. This phenomenon is evidently caused by the skewed distribution of the fitted values. Notably, if the residual plot were evaluated through a visual test, it would not be rejected since the true residual plot positioned at 10 can not be distinguished from the others.

Moving forward, we will employ the trained computer vision model to assess the residual plot with the assistance of the `autovi` R package. This package is accessible on the GitHub repository `TengMCing/autovi`, and users can install it by executing the command `remotes::install_github("TengMCing/autovi")` in R.

The results of the `list_keras_model()` function provide a list of available trained computer vision models. To perform the residual plot assessment, users need to supply a fitted linear regression model and select a trained Keras model to initialize the checker.

```
checker <- auto_vi(fitted_mod = mod,
                     keras_mod = get_keras_model("vss_phn_32"))
```

When invoking the `check()` method to execute the assessment, users can specify the number of null plots and bootstrapped samples using the `null_draws` and `boot_draws` arguments, respectively. The diagnostic results can be viewed by directly printing the object. Alternatively, a summary plot of the assessment can be generated using the `summary_plot()` method.

```
checker$check(null_draws = 200L, boot_draws = 200L)
checker$summary_plot()
```

Figure 17 presents the results of the assessment by the computer vision model. Notably, the observed visual signal strength is considerably lower than the 95% sample quantile of the null distribution. Moreover, the bootstrapped distribution suggests that it is highly improbable for the fitted model to be misspecified as the majority of bootstrapped fitted models will not be rejected. Thus, for this particular fitted model, both the visual test and the computer vision model will not reject H_0 . However, the Breusch-Pagan test will reject H_0 because it can not effectively utilize information

from null plots.

The attention map at plot B of Figure 17 suggests that the estimation is highly influenced by the top-right and bottom-right part of the residual plot, as it forms two vertices of the triangular shape. A principle component analysis is also performed on the output of the global pooling layer of the computer vision model. As mentioned in Simonyan and Zisserman (2014), a computer vision model built upon the convolutional blocks can be viewed as a feature extractor. For the 32×32 model, there are 256 features outputted from the global pooling layer, which can be further used for different visual tasks not limited to distance prediction. To see if these features can be effectively used for distinguishing null plots and true residual plot, we linearly project them into the PC1 vs PC2 space as shown in Figure 17. It can be observed that because the bootstrapped plots are mostly similar to the null plots, the points drawn in different colours are mixed together. The true residual plot is also covered by both the cluster of null plots and cluster of bootstrapped plots. This accurately reflects our understanding of Figure 18.

11.2. *Boston housing*

The Boston housing dataset, originally published by Harrison Jr and Rubinfeld (1978), offers insights into housing in the Boston, Massachusetts area. For illustration purposes, we will utilize a reduced version from Kaggle, comprising 489 rows and 4 columns: average number of rooms per dwelling (RM), percentage of lower status of the population (LSTAT), pupil-teacher ratio by town (PTRATIO), and Median value of owner-occupied homes in \$1000's (MEDV). In our analysis, MEDV will serve as the response variable, while the other columns will function as predictors in a linear regression model. Our primary focus is to detect non-linearity, because the relationships between RM and MEDV or LSTAT and MEDV are non-linear.

Figure 19 displays the residual plot and the assessment conducted by the computer vision model. A clear non-linearity pattern resembling a “U” shape is shown in the plot A. Furthermore, the RESET test yields a very small p -value. The estimated distance \hat{D} significantly exceeds $Q_{null}(0.95)$, leading to rejection of H_0 . The bootstrapped distribution also suggests that almost all the bootstrapped fitted models will be rejected,

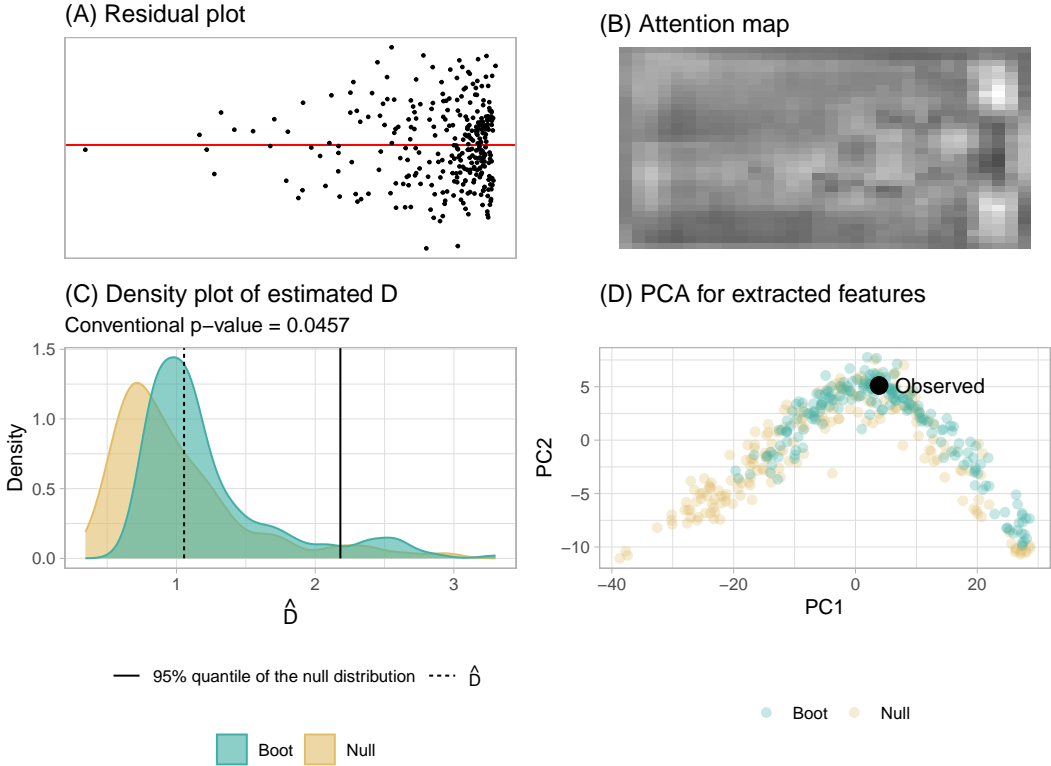


Figure 17. A summary of the residual plot assessment evaluated on 200 null plots and 200 bootstrapped plots. (A) The true residual plot exhibiting a “left-triangle” shape. (B) The attention map produced by computing the gradient of the output with respect to the greyscale input. (C) The density plot of estimated distance for null plots and bootstrapped plots. The blue area indicates the distribution of estimated distances for bootstrapped plots, while the yellow area represents the distribution of estimated distances for null plots. The fitted model will not be rejected since $\hat{D} < Q_{null}(0.95)$. (D) PC2 vs PC1 plot for features extracted from the global pooling layer of the computer vision model.

indicating that the fitted model is unlikely to be correctly specified. The attention map in plot B suggests the center of the image has higher leverage than other areas, and it is the turning point of the “U” shape. The principal component analysis provided in plot D shows two distinct clusters of data points, further underlines the visual differences between bootstrapped plots and null plots. This coincides the findings from Figure 20, where the true plot exhibiting a “U” shape is visually distinctive from null plots. If a visual test is conducted by human, H_0 will also be rejected.

11.3. *Datasaurus*

The computer vision model possesses the capability to detect not only typical issues like non-linearity, heteroskedasticity, and non-normality but also artifact visual pat-

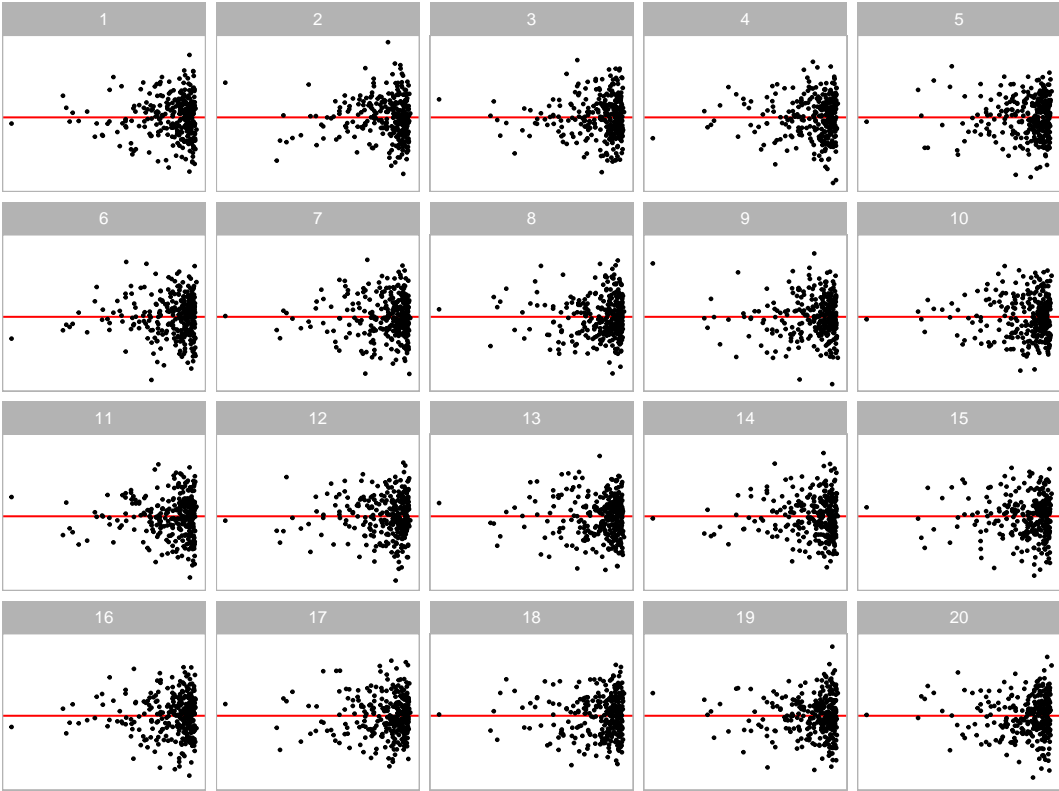


Figure 18. A lineup of residual plots displaying "left-triangle" visual patterns. The true residual plot occupies position 10, yet there are no discernible visual patterns that distinguish it from the other plots.

terns resembling real-world objects, as long as they do not appear in null plots. These visual patterns can be challenging to categorize in terms of model violations. Therefore, we will employ the RESET test, the Breusch-Pagan test, and the Shapiro-Wilk test (Shapiro and Wilk 1965) for comparison.

The "dino" dataset within the `datasaurus` R package exemplifies this scenario. With only two columns, x and y , fitting a regression model to this data yields a residual plot resembling a "dinosaur," as displayed in plot A of Figure 21. Unsurprisingly, this distinct residual plot stands out in a lineup, as shown in Figure 22. A visual test conducted by humans would undoubtedly reject H_0 .

According to the residual plot assessment by the computer vision model, \hat{D} exceeds $Q_{null}(0.95)$, warranting a rejection of H_0 . Additionally, most of the bootstrapped fitted models will be rejected, indicating a misspecified model. However, both the RESET test and the Breusch-Pagan test yield p -values greater than 0.3, leading to a non-rejection of H_0 . Only the Shapiro-Wilk test rejects the normality assumption with a

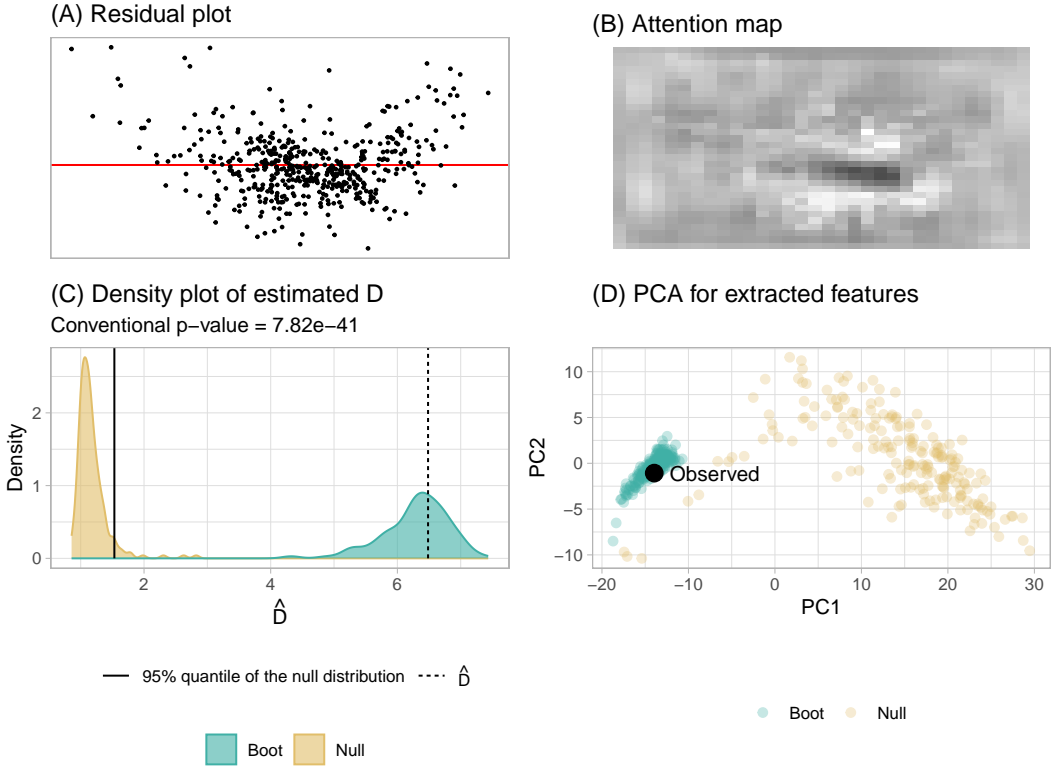


Figure 19. A summary of the residual plot assessment for the Boston housing fitted model evaluated on 200 null plots and 200 bootstrapped plots. (A) The true residual plot exhibiting a “U” shape. (B) The attention map produced by computing the gradient of the output with respect to the greyscale input. (C) The density plot of estimated distance for null plots and bootstrapped plots. The blue area indicates the distribution of estimated distances for bootstrapped plots, while the yellow area represents the distribution of estimated distances for null plots. The fitted model will be rejected since $\hat{D} \geq Q_{null}(0.95)$. (D) PC2 vs PC1 plot for features extracted from the global pooling layer of the computer vision model.

small p -value.

More importantly, the attention map in plot B of Figure 21 clearly exhibits a “dinosaur” shape, strongly suggesting the prediction of the distance is based on human perceptible visual patterns. The computer vision model is also capable of capturing the contour or the outline of the embedded shape, just like human being reading residual plots. The principle component analysis in plot D of Figure 21 also shows that the cluster of bootstrapped plots is at the corner of the cluster of null plots.

More importantly, the attention map in plot B of Figure 21 clearly exhibits a “dinosaur” shape, strongly suggesting that the distance prediction is based on human-perceptible visual patterns. The computer vision model effectively captures the contour or outline of the embedded shape, similar to how humans interpret residual plots. Additionally, the principal component analysis in plot D of Figure 21 demonstrates that

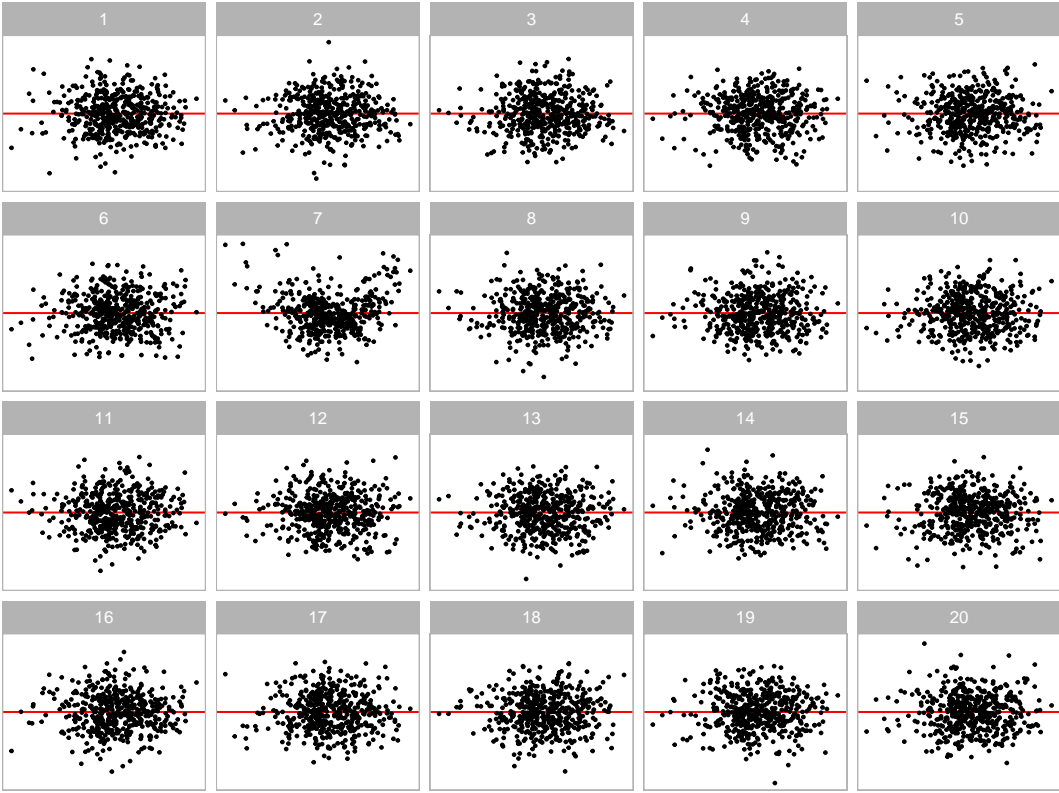


Figure 20. A lineup of residual plots for the Boston housing fitted model. The true residual plot is at position 7. It can be easily identified as the most different plot.

the cluster of bootstrapped plots is positioned at the corner of the cluster of null plots.

In practice, without accessing the residual plot, it would be challenging to identify the artificial pattern of the residuals. Moreover, conducting a normality test for a fitted regression model is not always standard practice among analysts. Even when performed, violating the normality assumption is sometimes deemed acceptable, especially considering the application of quasi-maximum likelihood estimation in linear regression. This example underscores the importance of evaluating residual plots and highlights how the proposed computer vision model can facilitate this process.

12. Limitations and Future Work

Despite the computer vision model performing well with general cases under the synthetic data generation scheme and the three examples used in this paper, this study has several limitations that could guide future work.

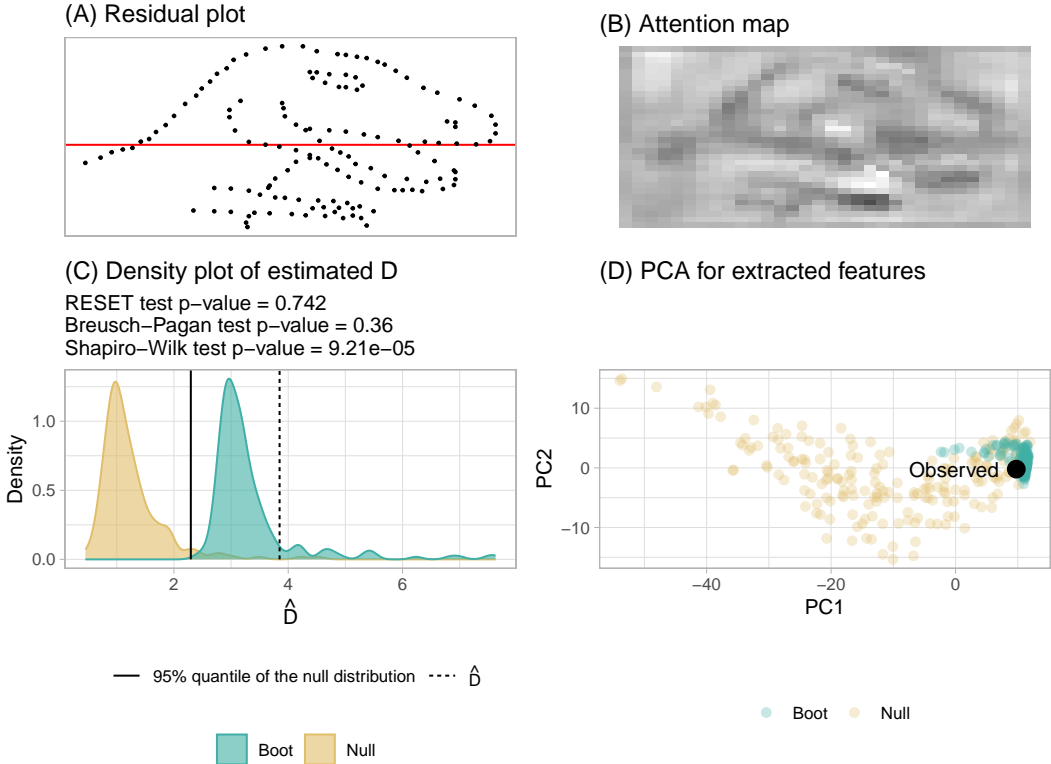


Figure 21. A summary of the residual plot assessment for the Datasaurus fitted model evaluated on 200 null plots and 200 bootstrapped plots. (A) The true residual plot exhibiting a "dinosaur" shape. (B) The attention map produced by computing the gradient of the output with respect to the greyscale input. (C) The density plot of estimated distance for null plots and bootstrapped plots. The blue area indicates the distribution of estimated distances for bootstrapped plots, while the yellow area represents the distribution of estimated distances for null plots. The fitted model will be rejected since $\hat{D} \geq Q_{null}(0.95)$. (D) PC2 vs PC1 plot for features extracted from the global pooling layer of the computer vision model.

The proposed distance measure assumes that the true model is a classical normal linear regression model, which can be too restrictive. Although this paper does not address the relaxation of this assumption, there are potential methods to evaluate other types of regression models. The most comprehensive approach would be to define a distance measure for each different class of regression model and then train the computer vision model following the methodology described in this paper. To accelerate training, one could use the convolutional blocks of our trained model as a feature extractor and perform transfer learning on top of it, as these blocks effectively capture shapes in residual plots. Another approach would be to transform the residuals so they are roughly normally distributed and have constant variance. If only raw residuals are used, the distance-based statistical testing compares the difference in distance to a classical normal linear regression model for the true plot and null plots. This com-

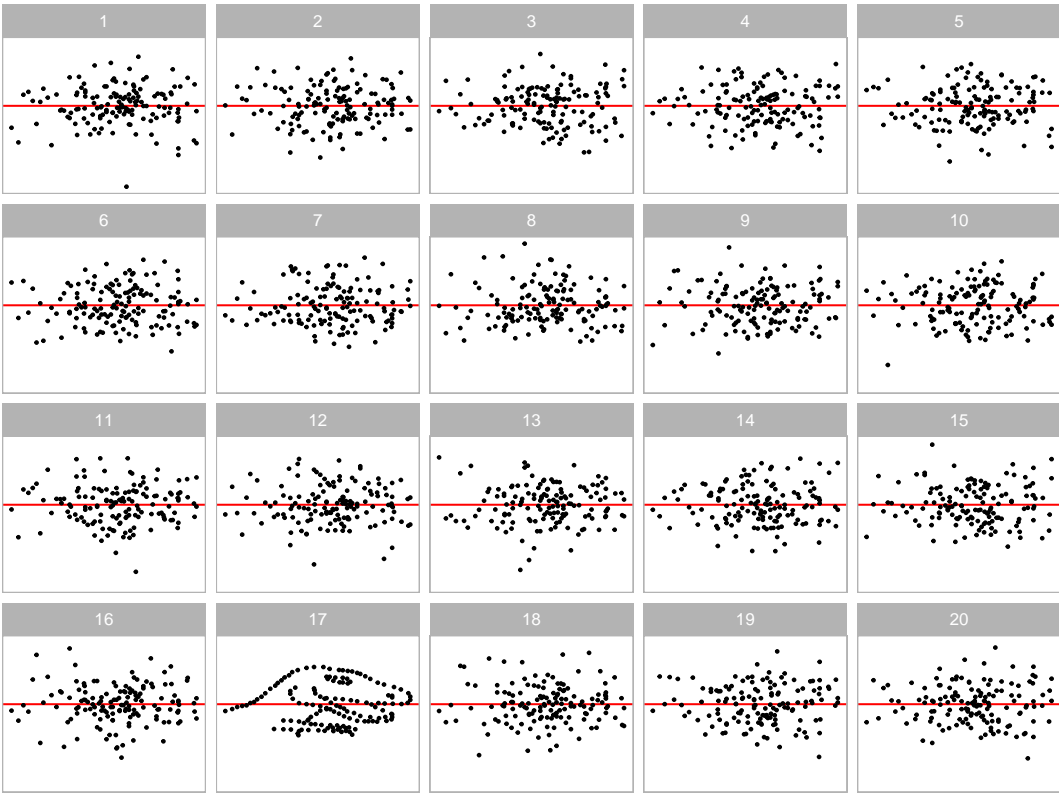


Figure 22. A lineup of residual plots for the fitted model on the "dinosaur" dataset. The true residual plot is at position 17. It can be easily identified as the most different plot as the visual pattern is extremely artificial.

parison is meaningful only if the difference can be identified by the distance measure proposed in this paper.

There are other types of residual plots commonly used in diagnostics, such as residuals vs. predictor and quantile-quantile plots. In this study, we focused on the most commonly used residual plot as a starting point for exploring the new field of automated visual inference. Similarly, we did not explore other, more sophisticated computer vision model architectures and specifications for the same reason. While the performance of the computer vision model is acceptable, there is still room for improvement to achieve behavior more closely resembling that of humans interpreting residual plots. This may require external survey data or human subject experiment data to understand the fundamental differences between our implementation and human evaluation.

13. Conclusion

In this study, we have introduced a distance measure based on Kullback-Leibler divergence to quantify the disparity between the residual distribution of a fitted classical normal linear regression model and the reference residual distribution assumed under correct model specification. This distance measure effectively captures the magnitude of model violations in misspecified models. We propose a computer vision model to estimate this distance, utilizing the residual plot of the fitted model as input. The resulting estimated distance serves as the foundation for constructing a single Model Violation Index (MVI), facilitating the quantification of various model violations.

Moreover, the estimated distance enables the development of a formal statistical testing procedure by evaluating a large number of null plots generated from the fitted model. Additionally, employing bootstrapping techniques and refitting the regression model allows us to ascertain how frequently the fitted model is considered misspecified if data were repeatedly obtained from the same data generating process.

The trained computer vision model demonstrates strong performance on both the training and test sets, although it exhibits slightly lower performance on residual plots with non-linearity visual patterns compared to other types of violations. The statistical tests relying on the estimated distance predicted by the computer vision model exhibit lower sensitivity compared to conventional tests but higher sensitivity compared to visual tests conducted by humans. While the estimated distance generally mirrors the strength of the visual signal perceived by humans, there remains scope for further improvement in its performance.

Several examples are provided to showcase the effectiveness of the proposed method across different scenarios, emphasizing the similarity between visual tests and distance-based tests. Overall, both visual tests and distance-based tests can be viewed as combined tests, aiming to assess the correctness of all model assumptions collectively. In contrast, individual residual diagnostic tests such as the RESET test and the Breusch-Pagan test only evaluate specific model assumptions. In practice, selecting an appropriate set of statistical tests for regression diagnostics can be challenging, particularly given the necessity of adjusting the significance level for each test.

Our method holds significant value as it helps alleviate a portion of analysts' work-load associated with assessing residual plots. While we recommend analysts to continue reading residual plots whenever feasible, as they offer invaluable insights, our approach serves as a valuable tool for automating the diagnostic process or for supplementary purposes when needed.

Acknowledgements

These R packages were used for the work: `tidyverse` (Wickham et al. 2019), `lmtest` (Zeileis and Hothorn 2002), `mpoly` (Kahle 2013), `ggbasic` (Jeppson, Hofmann, and Cook 2021), `kableExtra` (Zhu 2021), `patchwork` (Pedersen 2022), `cassowaryr` (Mason et al. 2022), `bandicoot` (Li 2024), `ggpcp` (Hofmann, VanderPlas, and Ge 2022), `keras` (Allaire and Chollet 2023) and `here` (Müller 2020).

The article was created with R packages `rticles` (Allaire et al. 2022), `knitr` (Xie 2014) and `rmarkdown` (Xie, Dervieux, and Riederer 2020). The project's GitHub repository (https://github.com/TengMCing/auto_residual_reading/paper) contains all materials required to reproduce this article.

Disclosure Statement

No potential conflict of interest was reported by the author(s).

Supplementary Materials

Appendix: The appendix includes more details about the neural network layers used for constructing the computer vision models.

References

- Abadi, Martín, Ashish Agarwal, Paul Barham, Eugene Brevdo, Zhifeng Chen, Craig Citro, Greg S Corrado, et al. 2016. “Tensorflow: Large-scale machine learning on heterogeneous distributed systems.” *arXiv preprint arXiv:1603.04467* .

- Allaire, JJ, and François Chollet. 2023. *keras: R Interface to 'Keras'*. R package version 2.13.0, <https://CRAN.R-project.org/package=keras>.
- Allaire, JJ, Yihui Xie, Christophe Dervieux, R Foundation, Hadley Wickham, Journal of Statistical Software, Ramnath Vaidyanathan, et al. 2022. *rticles: Article formats for R Markdown*. R package version 0.24, <https://CRAN.R-project.org/package=rticles>.
- Belsley, David A, Edwin Kuh, and Roy E Welsch. 1980. *Regression diagnostics: Identifying influential data and sources of collinearity*. John Wiley & Sons.
- Breusch, Trevor S, and Adrian R Pagan. 1979. “A simple test for heteroscedasticity and random coefficient variation.” *Econometrica: Journal of the Econometric Society* 1287–1294.
- Brunetti, Antonio, Domenico Buongiorno, Gianpaolo Francesco Trotta, and Vitoantonio Bevilacqua. 2018. “Computer vision and deep learning techniques for pedestrian detection and tracking: A survey.” *Neurocomputing* 300: 17–33.
- Buja, Andreas, Dianne Cook, Heike Hofmann, Michael Lawrence, Eun-Kyung Lee, Deborah F Swayne, and Hadley Wickham. 2009. “Statistical inference for exploratory data analysis and model diagnostics.” *Philosophical Transactions of the Royal Society A: Mathematical, Physical and Engineering Sciences* 367 (1906): 4361–4383.
- Chen, Yun, Shijie Su, and Hui Yang. 2020. “Convolutional neural network analysis of recurrence plots for anomaly detection.” *International Journal of Bifurcation and Chaos* 30 (01): 2050002.
- Chollet, François, et al. 2015. “Keras.” <https://keras.io>.
- Chopra, Sumit, Raia Hadsell, and Yann LeCun. 2005. “Learning a similarity metric discriminatively, with application to face verification.” In *2005 IEEE computer society conference on computer vision and pattern recognition (CVPR'05)*, Vol. 1, 539–546. IEEE.
- Chowdhury, Niladri Roy, Dianne Cook, Heike Hofmann, and Mahbubul Majumder. 2018. “Measuring lineup difficulty by matching distance metrics with subject choices in crowd-sourced data.” *Journal of Computational and Graphical Statistics* 27 (1): 132–145.
- Chu, Hongyang, Xinwei Liao, Peng Dong, Zhiming Chen, Xiaoliang Zhao, and Jiandong Zou. 2019. “An automatic classification method of well testing plot based on convolutional neural network (CNN).” *Energies* 12 (15): 2846.
- Cook, R Dennis, and Sanford Weisberg. 1982. *Residuals and influence in regression*. New York: Chapman and Hall.
- Emami, Shervin, and Valentin Petrut Suciu. 2012. “Facial recognition using OpenCV.” *Journal of Mobile, Embedded and Distributed Systems* 4 (1): 38–43.

- Frisch, Ragnar, and Frederick V Waugh. 1933. “Partial time regressions as compared with individual trends.” *Econometrica: Journal of the Econometric Society* 387–401.
- Fukushima, Kunihiko, and Sei Miyake. 1982. “Neocognitron: A new algorithm for pattern recognition tolerant of deformations and shifts in position.” *Pattern recognition* 15 (6): 455–469.
- Goscinski, Wojtek J, Paul McIntosh, Ulrich Felzmann, Anton Maksimenko, Christopher J Hall, Timur Gureyev, Darren Thompson, et al. 2014. “The multi-modal Australian ScienceS Imaging and Visualization Environment (MASSIVE) high performance computing infrastructure: applications in neuroscience and neuroinformatics research.” *Frontiers in Neuroinformatics* 8: 30.
- Hailesilassie, Tameru. 2019. “Financial Market Prediction Using Recurrence Plot and Convolutional Neural Network.” .
- Harrison Jr, David, and Daniel L Rubinfeld. 1978. “Hedonic housing prices and the demand for clean air.” *Journal of environmental economics and management* 5 (1): 81–102.
- Hastie, Trevor J. 2017. “Generalized additive models.” In *Statistical models in S*, 249–307. Routledge.
- Hatami, Nima, Yann Gavet, and Johan Debayle. 2018. “Classification of time-series images using deep convolutional neural networks.” In *Tenth international conference on machine vision (ICMV 2017)*, Vol. 10696, 242–249. SPIE.
- Hermite, M. 1864. *Sur un nouveau développement en série des fonctions*. Imprimerie de Gauthier-Villars.
- Hofmann, Heike, Susan VanderPlas, and Yawei Ge. 2022. *ggpcp: Parallel Coordinate Plots in the 'ggplot2' Framework*. R package version 0.2.0, <https://CRAN.R-project.org/package=ggpcp>.
- Hyndman, Rob J, and Yanan Fan. 1996. “Sample quantiles in statistical packages.” *The American Statistician* 50 (4): 361–365.
- Jeppson, Haley, Heike Hofmann, and Di Cook. 2021. *ggbmosaic: Mosaic plots in the 'ggplot2' framework*. R package version 0.3.3, <https://CRAN.R-project.org/package=ggbmosaic>.
- Kahle, David. 2013. “mpoly: Multivariate Polynomials in R.” *The R Journal* 5 (1): 162–170.
- Krishnan, Ganesh, and Heike Hofmann. 2021. “Hierarchical Decision Ensembles-An inferential framework for uncertain Human-AI collaboration in forensic examinations.” *arXiv preprint arXiv:2111.01131* .
- Kullback, Solomon, and Richard A Leibler. 1951. “On information and sufficiency.” *The Annals*

- of Mathematical Statistics* 22 (1): 79–86.
- Langsrud, Øyvind. 2005. “Rotation tests.” *Statistics and computing* 15: 53–60.
- Lee, Howard, and Yi-Ping Phoebe Chen. 2015. “Image based computer aided diagnosis system for cancer detection.” *Expert Systems with Applications* 42 (12): 5356–5365.
- Li, Weihao. 2024. “bandicoot: Light-Weight Python-Like Object-Oriented System.” <https://CRAN.R-project.org/package=bandicoot>.
- Li, Weihao, Dianne Cook, Emi Tanaka, and Susan VanderPlas. 2023. “A Plot is Worth a Thousand Tests: Assessing Residual Diagnostics with the Lineup Protocol.” *arXiv preprint arXiv:2308.05964* .
- Loy, Adam, and Heike Hofmann. 2013. “Diagnostic tools for hierarchical linear models.” *Wiley Interdisciplinary Reviews: Computational Statistics* 5 (1): 48–61.
- Loy, Adam, and Heike Hofmann. 2014. “HLMdiag: A suite of diagnostics for hierarchical linear models in R.” *Journal of Statistical Software* 56: 1–28.
- Loy, Adam, and Heike Hofmann. 2015. “Are you normal? The problem of confounded residual structures in hierarchical linear models.” *Journal of Computational and Graphical Statistics* 24 (4): 1191–1209.
- Mason, Harriet, Stuart Lee, Ursula Laa, and Dianne Cook. 2022. *cassowaryr: Compute Scagnostics on Pairs of Numeric Variables in a Data Set*. R package version 2.0.0, <https://CRAN.R-project.org/package=cassowaryr>.
- Müller, Kirill. 2020. *here: A simpler way to find your files*. R package version 1.0.1, <https://CRAN.R-project.org/package=here>.
- Ojeda, Sun Arthur A, Geoffrey A Solano, and Elmer C Peramo. 2020. “Multivariate time series imaging for short-term precipitation forecasting using convolutional neural networks.” In *2020 International Conference on Artificial Intelligence in Information and Communication (ICAICC)*, 33–38. IEEE.
- O’Malley, Tom, Elie Bursztein, James Long, François Chollet, Haifeng Jin, Luca Invernizzi, et al. 2019. “Keras Tuner.” <https://github.com/keras-team/keras-tuner>.
- Pedersen, Thomas Lin. 2022. *patchwork: The composer of plots*. R package version 1.1.2, <https://CRAN.R-project.org/package=patchwork>.
- Ramsey, James Bernard. 1969. “Tests for specification errors in classical linear least-squares regression analysis.” *Journal of the Royal Statistical Society: Series B (Methodological)* 31 (2): 350–371.
- Rawat, Waseem, and Zenghui Wang. 2017. “Deep convolutional neural networks for image

- classification: A comprehensive review.” *Neural computation* 29 (9): 2352–2449.
- Shapiro, Samuel Sanford, and Martin B Wilk. 1965. “An analysis of variance test for normality (complete samples).” *Biometrika* 52 (3/4): 591–611.
- Silverman, Bernard W. 2018. *Density estimation for statistics and data analysis*. Routledge.
- Simonyan, Karen, and Andrew Zisserman. 2014. “Very deep convolutional networks for large-scale image recognition.” *arXiv preprint arXiv:1409.1556* .
- Singh, Karamjit, Garima Gupta, Lovekesh Vig, Gautam Shroff, and Puneet Agarwal. 2017. “Deep convolutional neural networks for pairwise causality.” *arXiv preprint arXiv:1701.00597* .
- Tukey, John W, and Paul A Tukey. 1985. “Computer graphics and exploratory data analysis: An introduction.” In *Proceedings of the sixth annual conference and exposition: computer graphics*, Vol. 85, 773–785.
- Vo, Nam N, and James Hays. 2016. “Localizing and orienting street views using overhead imagery.” In *Computer Vision–ECCV 2016: 14th European Conference, Amsterdam, The Netherlands, October 11–14, 2016, Proceedings, Part I* 14, 494–509. Springer.
- Wang, Zhou, Alan C Bovik, Hamid R Sheikh, and Eero P Simoncelli. 2004. “Image quality assessment: from error visibility to structural similarity.” *IEEE transactions on image processing* 13 (4): 600–612.
- Wickham, Hadley, Mara Averick, Jennifer Bryan, Winston Chang, Lucy D’Agostino McGowan, Romain François, Garrett Grolemund, et al. 2019. “Welcome to the tidyverse.” *Journal of Open Source Software* 4 (43): 1686.
- Widen, Holly M, James B Elsner, Stephanie Pau, and Christopher K Uejio. 2016. “Graphical inference in geographical research.” *Geographical Analysis* 48 (2): 115–131.
- Wilkinson, Leland, Anushka Anand, and Robert Grossman. 2005. “Graph-theoretic scagnostics.” In *Information Visualization, IEEE Symposium on*, 21–21. IEEE Computer Society.
- Xie, Yihui. 2014. “knitr: A comprehensive tool for reproducible research in R.” In *Implementing reproducible computational research*, edited by Victoria Stodden, Friedrich Leisch, and Roger D. Peng. Chapman and Hall/CRC. ISBN 978-1466561595, <http://www.crcpress.com/product/isbn/9781466561595>.
- Xie, Yihui, Christophe Dervieux, and Emily Riederer. 2020. *R Markdown cookbook*. Boca Raton, Florida: Chapman and Hall/CRC. ISBN 9780367563837, <https://bookdown.org/yihui/rmarkdown-cookbook>.
- Zeileis, Achim, and Torsten Hothorn. 2002. “Diagnostic checking in regression relationships.”

R News 2 (3): 7–10.

Zhang, Ye, Yi Hou, Shilin Zhou, and Kewei Ouyang. 2020. “Encoding time series as multi-scale signed recurrence plots for classification using fully convolutional networks.” *Sensors* 20 (14): 3818.

Zhu, Hao. 2021. *kableExtra: Construct complex table with kable and pipe syntax*. R package version 1.3.4, <https://CRAN.R-project.org/package=kableExtra>.